Author/s:
Morón, S;Kohn, BP;Beucher, R;Mackintosh, V;Cawood, PA;Moresi, L;Gallagher, SJ

Title:
Denuding a Craton: Thermochronology Record of Phanerozoic Unroofing from the Pilbara Craton, Australia

Date:
2020

Citation:
Morón, S., Kohn, B. P., Beucher, R., Mackintosh, V., Cawood, P. A., Moresi, L. & Gallagher, S. J. (2020). Denuding a Craton: Thermochronology Record of Phanerozoic Unroofing from the Pilbara Craton, Australia. Tectonics, 39 (9), https://doi.org/10.1029/2019tc005988.

Persistent Link:
https://hdl.handle.net/11343/248119

Tectonics

RESEARCH ARTICLE
10.1029/2019TC005988

Key Points:

- Pilbara Craton basement records a widespread cooling episode mainly between ~420 and 300 Ma resulting from denudation of a sedimentary cover
- Denudation is related to rifting adjacent to the craton associated with far-field intraplate deformation transmitted over hundreds of kilometers
- Differences in unroofing estimates and timing are related to the thermal effect and variable thickness of the sedimentary blanket

Supporting Information:

- Supporting Information S1
- Data Set S1

Correspondence to:
S. Morón,
sara.moronpolanco@sydney.edu.au

Citation:
Morón, S., Kohn, B. P., Beucher, R., Mackintosh, V., Cawood, P. A., Moresi, L., & Gallagher, S. J. (2020). Denuding a craton: Thermochronology record of Phanerozoic unroofing from the Pilbara Craton, Australia. *Tectonics*, *39*, e2019TC005988. https://doi.org/10.1029/2019TC005988

Received 17 NOV 2019
Accepted 10 AUG 2020
Accepted article online 16 AUG 2020

Denuding a Craton: Thermochronology Record of Phanerozoic Unroofing From the Pilbara Craton, Australia

Sara Morón[1,2], Barry P. Kohn[1], Romain Beucher[1,3], Vhairi Mackintosh[1], Peter A. Cawood[4], Louis Moresi[1,3], and Stephen J. Gallagher[1]

[1]School of Earth Sciences, University of Melbourne, Parkville, Victoria, Australia, [2]EarthByte Group, School of Geosciences, University of Sydney, Camperdown, New South Wales, Australia, [3]Research School of Earth Sciences, Australian National University, Canberra, Australian Capital Territory, Australia, [4]School of Earth, Atmosphere and Environment, Monash University, Melbourne, Victoria, Australia

Abstract Cratons are ancient regions of relatively stable continental fragments considered to have attained long-term tectonic and geomorphic stability. Low-temperature thermochronology data, however, suggest that some cratons have experienced discrete Phanerozoic heating and cooling episodes. We report apatite fission track, and apatite and zircon (U-Th)/He low-temperature thermochronology data from the Archean Pilbara craton and adjacent Paleoproterozoic basement, NW Australia. Inverse thermal history simulations of this spatially extensive data set reveal that the region has experienced ~50–70°C cooling, which is interpreted as a response to the unroofing of erodible strata overlying basement. The timing of cooling onset is variable, mainly ~420–350 Ma in the southern and central Pilbara-eastern Hamersley Basin and ~350–300 Ma in the northern Pilbara, while the westernmost Pilbara-central Hamersley Basin does not record a significant Paleozoic cooling event. These differences are attributed to variations in sedimentary thickness and proximity to adjacent rift basins, which lack Archean age zircons in their Paleozoic strata. The onset of Paleozoic cooling coincides with the timing of the episodic intraplate late Ordovician-Carboniferous Alice Springs Orogeny. This orogeny is thought to have resulted from far-field plate margin stresses, which in turn caused the opening of the adjacent Canning Basin, to the north and east of the craton. We propose that basin development triggered a change of base level, resulting in denudation and the crustal cooling event reported here. Our results provide further evidence for the transmission of far-field forces to cratons over hundreds of kilometers and support the view that cratons have experienced geomorphic changes during the Phanerozoic.

1. Introduction

Archean cratons make up less than 15% of continental areas (Bowring & Williams, 1999; Cawood et al., 2013; Goodwin, 1996), yet they are ubiquitous nuclei of many tectonic plate interiors (e.g., de Wit et al., 1992). Their long-term survival is mainly attributed to their thicker lithosphere, characterized by a relatively cool but compositionally buoyant upper-mantle keel (e.g., Jordan, 1978). Apart from some tectonic reworking near their margins (e.g., Lenardic et al., 2000; Mackintosh et al., 2019), cratonization has often been viewed as the end point in the evolution of continental lithosphere, after which it enters a relatively quiescent state (e.g., Pollack, 1986). A number of recent works, however, including some low-temperature thermochronology studies, indicate that the uppermost few kilometers of cratonic crust may record evidence for widespread, discrete Neoproterozoic and/or Phanerozoic heating and cooling episodes (e.g., Ault et al., 2009, 2013; Baughman & Flowers, 2018; Danišík et al., 2008; Enkelmann & Garver, 2016; Feinstein et al., 2009; Flowers et al., 2006; Flowers & Schoene, 2010; Guenthner et al., 2017; Kasanzu, 2017; Kohn et al., 2005; Kohn & Gleadow, 2019; Larson et al., 1999; Mackintosh et al., 2017; Wildman et al., 2017). Such episodes have often been interpreted as being related to a record of burial and erosion, even though conventional stratigraphic and/or structural controls are often absent.

Low-temperature thermochronology radiometric dating methods, characterized by temperature sensitive daughter products that accumulate in minerals, are retained over a range of temperatures (< ~300°C) (e.g., Enkelmann & Garver, 2016). Within the upper crustal environment, temperature can often be used

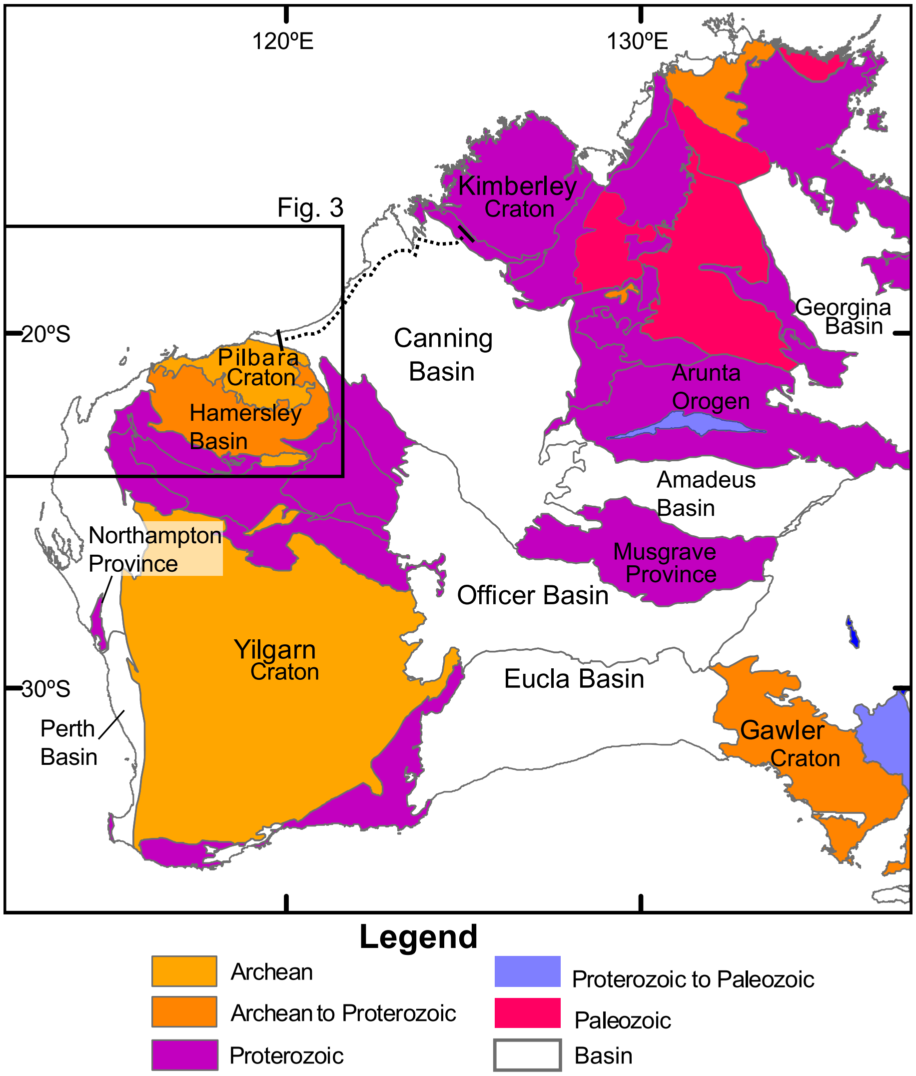

Figure 1. Western and central Australia geological domains grouped by age and the location of basins adjacent to the Pilbara Craton (data from Geoscience Australia, http://www.ga.gov.au/nationaldatasetsgis/). The dashed line shows the line traversed for the seismic section in Figure 2. The black rectangle outlines the study area shown in more detail in Figure 3.

as a proxy for depth, so that reconstructed thermal histories may reveal a record of rock movement toward the surface, which may reflect tectonic and landscape evolution processes. The unique ability of low-temperature thermochronology systems to detect and quantify the signature of such movements or thermal perturbations in the near surface environment over geological time scales, which are largely invisible to other analytical techniques, has been the basis for their application to a broad range of interdisciplinary problems in the Earth Sciences (e.g., Gleadow et al., 2002; Reiners et al., 2018).

From a landscape evolution perspective, a key question linked to low-temperature thermochronology investigations on cratons is to what degree that thermal history information can improve our general understanding of patterns of exhumation, weathering, climate, biogeochemical cycling, and ocean-land sediment budgets (e.g., Alessio et al., 2019; Belton & Raab, 2010; Danišík et al., 2008; Kohn & Gleadow, 2019; Lee et al., 2018). Furthermore, these analyses can help elucidate the potential preservation of immensely valuable mineral resources, which these terranes often host. Within this context, we have carried out a low-temperature thermochronology study of the resource-rich Archean Pilbara Craton and adjacent terranes of northwest Australia (Figure 1). This investigation includes inverse thermal history modeling based on a spatially extensive (~118,000 km^2) low-temperature thermochronology data set and incorporates geochronological data from earlier studies carried out on some of the same samples studied in this work. The onset of the cooling episode reported here is coeval with an intraplate tectonic event that has been proposed to have caused the opening of basins adjacent to the craton (Roberts & Houseman, 2001). We propose that basin opening triggered a change in base level and subsequently caused denudation that generated the crustal cooling reported here. This study showcases how the effects of far-field deformation can be transmitted to cratons over hundreds of kilometers and substantiates the notion that cratons have been geomorphologically active during the Phanerozoic.

2. Geological Setting

The Archean Pilbara Craton, located in the northwestern corner of Australia, extends over an area of ~60,000 km^2 (Figure 1). It is surrounded by Early Archean-Paleoproterozoic basins to the south and Phanerozoic basins to the west, north, and east (Figure 1). The craton is composed of early crust (3.80–3.53 Ga), granite-greenstone terranes (3.53–3.07 Ga), volcano-sedimentary basins (3.05–2.93 Ga), and post-orogenic granites (2.89–2.83 Ga) (Hickman & Van Kranendonk, 2012). Late Archean-Paleoproterozoic basins to the south contain a succession of interbedded clastic and chemical sedimentary rocks and volcanic rocks. This succession has been associated with a history of crustal extension and volcanic plateau formation (Fortescue Group), through passive margin settings (2.63–2.45 Ga Hamersley Group), to basin deposition (<2.45 to >2.21 Ga, Turee Creek Group; Hickman & Van Kranendonk, 2012). The Gascoyne Complex is a Paleoproterozoic terrane of granite and medium- to high-grade metamorphic rocks that outcrops to the southwest of the Pilbara Craton at the western end of the Capricorn Orogen. The orogen forms an ~1,000 km arcuate belt of variably metamorphosed and deformed rocks between the Pilbara craton to the north and the Yilgarn Craton to the south. It is interpreted to record Paleoproterozoic collision between the two cratons (to form the West Australian Craton), which corresponds with a major phase of global supercontinent assembly (Cawood & Tyler, 2004).

Stromatolite-bearing sedimentary strata of the Fortescue Group in the Hamersley Basin to the south of the Pilbara Craton suggest the region was close to sea level at ~2.7 Ga (Flament et al., 2011). The present-day Pilbara craton lies at elevations <800 m and lacks any overlying Neoproterozoic-Phanerozoic sedimentary cover.

Basin formation and infilling adjacent to the Pilbara Craton (Figure 1) occurred from the Early Ordovician to the Early Cretaceous (Hashimoto et al., 2018; Kennard et al., 1994; Shaw et al., 1995). In the Canning Basin, adjacent to the craton, Lower Paleozoic sedimentary packages range between 1 and 2.5 km thick (Figure 2) (Hashimoto et al., 2018). Glacially striated basement rocks (mostly in the northeastern Pilbara) and intraformational glacial striae in Permian sandstone provide evidence that glacial erosion related to the pervasive Permo-Carboniferous glaciation of Gondwana extended as far as the Pilbara Craton and the onshore Canning Basin (Gzhelian-Sakmarian ca. 305–285 Ma; Mory et al., 2008). Deformation phases recorded in the basins are the result of intracratonic tectonism, as well as multiple extension and sagging events (e.g., Driscoll & Karner, 1998; Gartrell, 2000; Mory & Haines, 2013). East and north of the Pilbara Craton (e.g., Canning Basin), seismic data show lithospheric thinning and regional-scale faults toward and at the craton boundary (Figure 2). This deformation has been related to a late Ordovician-Carboniferous, polyphase intraplate tectonic event referred to as the Alice Springs Orogeny (e.g., Buick et al., 2008; Cartwright et al., 1999; Collins & Shaw, 1995; Glorie et al., 2017; Shaw et al., 1991). This event resulted from a combination of far-field stresses and the localization of deformation associated with thermal weakening or with regions of contrasting strengths (Camacho et al., 2002). Basins offshore of the Pilbara Craton formed as a result of multiple extension and sagging events (Driscoll & Karner, 1998; Gartrell, 2000). The first rifting phase, spanning the Late Carboniferous to Permian, is associated with the opening of the Neo-Tethys Ocean. Rifting was followed by a Triassic sagging event, during which a >4 km-thick fluvio-deltaic sequence accumulated (Martin et al., 2018; Morón et al., 2019). A second rifting phase, commencing in the Early Jurassic (Toarcian) and continuing until the Early Cretaceous (Valanginian), is associated with the breakup of Gondwana (I'Anson et al., 2019). Following the Santonian, the offshore region of the Pilbara Craton became a passive margin and has been tectonically quiescent since that time (I'Anson et al., 2019).

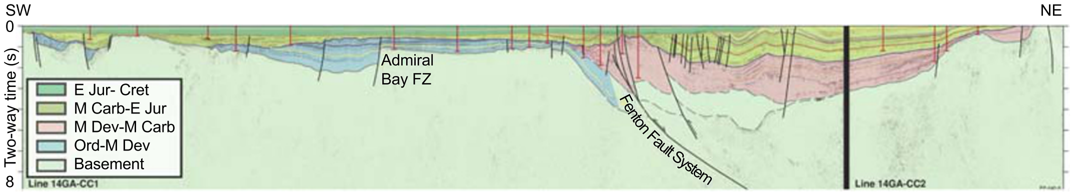

Figure 2. Stratigraphy across the Canning Basin along Lines 14GA-CC1 and 14GA-CC2 of the L205 Canning Coastal Deep Crustal Seismic Reflection Survey. Note how in the SW the 1–2.5 km-thick Ordovician to Devonian sedimentary packages are preferentially located close to the Pilbara Craton. Location of cross-section line is shown in Figure 1. Modified after Hashimoto et al. (2018).

3. Low-Temperature Thermochronology—Background

The three low-temperature thermochronology methods utilized in this work are apatite fission track (AFT), apatite (U-Th-Sm)/He (AHe), and zircon (U-Th)/He (ZHe) thermochronometry. The fundamental principles underpinning these techniques, interpretation of data, and applications are outlined in several works, for example, Gleadow et al. (2002) for AFT and Farley (2002) and Reiners et al. (2018) for AHe and ZHe.

Briefly, fission tracks are formed continuously under typical upper crustal temperature and pressure conditions but may be annealed (i.e., track lengths are shortened) if temperatures become sufficiently high for the thermal energy to allow the mineral lattice to begin to repair itself. The temperature range over which annealing occurs is termed the Partial Annealing Zone (PAZ). Above the higher temperature limit of this zone, any tracks formed are totally annealed in a relatively short period of time, so that no physical record of the tracks remains and ages are completely reset. Fission track annealing in apatite is a complex, nonlinear process, dominantly controlled by temperature (markedly > ~60°C), duration of heating, and to a lesser extent by crystallographic orientation (e.g., Donelick et al., 2005). Annealing is also influenced by the complex interplay of anion (Cl, F, OH) and cation substitutions (e.g., REE, Mn, Na, Mg, Fe, Sr, Fe, and Si), with Cl playing a primary role (Barbarand et al., 2003; Carlson et al., 1999; Green et al., 1989). Higher Cl content is associated with greater resistance to track annealing, often resulting in older ages (e.g., Barbarand et al., 2003; Burtner et al., 1994; Carlson et al., 1999; Green et al., 1989). The bulk track-etching rate of apatite, although considered to be a less precise parameter (e.g., Schneider & Issler, 2019), has also been proposed as a kinetic proxy for bulk chemical composition, and this involves measurement of Dpar—the mean etch-pit diameter measured parallel to the crystallographic *c* axis (e.g., Donelick et al., 2005).

Temperature is considered to be the dominant mechanism for annealing, but some nonthermal processes have also been proposed, for example, seasoning of tracks, pressure effects, and α-radiation enhanced annealing (REA) (Ketcham, 2019). Of particular relevance for this work is REA of fission tracks, a process proposed to result principally from the decay of ^{238}U and ^{232}Th operating at low temperatures (<60°C) in areas of prolonged thermo-tectonic stability such as cratons (Hendriks & Redfield, 2005). The case for REA, considered to have been overlooked previously, is partly based on inverse correlations between AFT grain age and U content from southern and central Fennoscandian shield (Finland) samples. Donelick et al. (2006) also reported a range of inverse relationships (weak to moderately strong) between AFT age and α-emitter actinides within samples from the Fennoscandian and Canadian shields, with the older grains from the former showing the strongest negative correlation.

The effect of the postulated REA, in addition to temperature sensitivity, implies that modeled AFT data in cratonic settings (and in U- and/or Th-rich apatites in general) using conventional thermal annealing models may lead to an overestimation of paleotemperatures, and hence the amount of any postulated overlying section removed. The applicability of REA to AFT studies in slowly cooled settings has been the subject of considerable debate (e.g., Donelick et al., 2006; Green & Duddy, 2006; Green et al., 2006; Hendriks & Redfield, 2006; Ketcham, 2019; Kohn et al., 2009; Larson et al., 2006; McDannell et al., 2019).

In the (U-Th)/He system, the He Partial Retention Zone (HePRZ) is a comparable concept to the PAZ. But in this case, it is related to the retention of the daughter ^{4}He, which can be lost progressively by volume diffusion over a range of temperatures (e.g., Farley, 2002). Above the higher temperature limits of the HePRZ, no helium is retained, and ages are totally reset.

Single grains analyzed for (U-Th)/He ages may significantly differ in their He diffusivity properties, thus contributing, to significant intersample age dispersion. Arguably, the greatest contribution to dispersion can be attributed to the effects of accumulation and distribution of α-radiation damage, grain size variation, and grain fragmentation (e.g., Danišík et al., 2017; Wildman et al., 2016). The relationship between single grain age and accumulated radiation damage and/or grain size on He diffusion has been shown to become markedly pronounced during thermal histories characterized by slow cooling, with prolonged residence in the HePRZ, or protracted reheating (e.g., Brown et al., 2013; Flowers & Kelley, 2011; Flowers et al., 2009; Gautheron et al., 2009; Reiners & Farley, 2001). For example, larger grain size will increase the diffusion length (Farley, 2002) leading to a positive relationship with age (e.g., Reiners & Farley, 2001). Radiation damage accumulation weights the decay of U and Th in terms of their α productivity and is commonly expressed as effective Uranium concentration, expressed as eU: [U ppm] + 0.235 * [Th ppm]. The damage creates defects and vacancies in the crystal structure, which may act as sites for He trapping (e.g., Flowers, 2009; Shuster et al., 2006) and He diffusion under high degrees of radiation damage (e.g., Guenthner et al., 2013). Therefore, in cratonic environments, owing to the long time span over which such damage may have accumulated, He data sets may possess a range of He diffusivities, and this may lead to relationships between He age and eU, which can be used to interpret data (e.g., Ault et al., 2009; Flowers, 2009; Flowers & Kelley, 2011; Guenthner et al., 2013). If apatite, for example, undergoes heating under sedimentary burial, then the He traps may undergo different degrees of annealing (self-repair) in accordance with the amount of radiation damage, and this will be further expressed in their capacity for He retention, leading to intrasample (U-Th)/He age dispersion (e.g., Chaumont et al., 2002; Gautheron et al., 2009; Recanati et al., 2017; Shuster et al., 2006).

Other possible factors that may contribute to (U-Th)/He age dispersion, but which may be more difficult to evaluate routinely, include eU zonation, the presence of eU-rich micro-inclusions, He implantation, and chemical composition. eU zonation has been claimed to rarely cause wide age dispersion in cratonic apatites beyond ~15% and that this range is commonly within the age deviations for AHe ages (e.g., Ault & Flowers, 2012), but that claim was more study specific and higher impacts of zoning have been demonstrated in other cratonic settings (e.g., Meesters & Dunai, 2002). If eU-rich microinclusions are present, and incompletely dissolved during the HNO_3 procedure prior to ICP-MS analysis, then the resulting parentless He might result in older ages (e.g., Vermeesch et al., 2007). He implantation from external sources, such as neighboring grains or thin grain coatings, is most pronounced in low eU ppm apatite grains (e.g., Danišík et al., 2010; Murray et al., 2014; Spiegel et al., 2009). The possible influence of apatite chemistry (principally Cl content) on He diffusion was discussed by Gautheron et al. (2013) and Djimbi et al. (2015) but was not deemed to have a significant effect in earlier studies where samples with a wide range of apatite Cl content were dated (House et al., 2000; Kohn, Foster, et al., 2002), or in a broader ranging work involving a multi-element apatite study (Recanati et al., 2017). He trapping in strained crystals (McDannell et al., 2018) and crystal imperfections, such as vacancy damage and crystallographic microvoids, may also lead to age dispersion by impeding He diffusion (Gerin et al., 2017; Zeitler et al., 2017). In zircons, fluid inclusions as potential He traps and detailed mapping of the heterogeneity of intragrain He and eU mapping also serve to further highlight potential sources of dispersed or anomalous (U-Th)/He ages (Danišík et al., 2017).

Corrections for α-ejection at grain boundaries are routinely applied in the (U-Th)/He system to account for the proportion of He lost based on the crystal surface to volume ratio (e.g., Farley et al., 1996; Gautheron et al., 2012; Hourigan et al., 2005; Ketcham et al., 2011). However, the application of this procedure in slowly cooled Archean/Paleoproterozoic rocks with a protracted diffusion history, such as those studied here, may lead to an overcorrection of the (U-Th)/He age (e.g., Danišík et al., 2008; Meesters & Dunai, 2002). In this work, for comparative purposes, the corrected AHe and ZHe ages are quoted throughout, but it is the uncorrected ages, which are input for the inverse thermal history modeling outlined in section 6, and it is the model outputs, which mainly inform the subsequent interpretations.

The thermochronometric systems used in this work cover a range of temperature sensitive ranges over which most annealing or He diffusion occurs. For the ZHe system, this temperature range is typically ~130–200°C (e.g., Wolfe & Stockli, 2010) but can also be considerably lower (<50°C) in strongly radiation damaged grains (e.g., Johnson et al., 2017). For AFT, it typically ranges from ~60–110°C (e.g., Gleadow et al., 2002), and for AHe it is ~30–90°C, depending on a number of factors such as the degree of accumulated radiation damage, grain size and grain fragmentation, and their effect on He diffusivity (e.g., Brown et al., 2013;

Djimbi et al., 2015; Flowers et al., 2009; Gautheron et al., 2009; Shuster et al., 2006). High eU apatites, with elevated levels of accumulated radiation damage however, show greater He retentivity such that AHe ages may be older than their coexisting AFT and ZHe ages and seemingly incompatible with expectations (e.g., Flowers & Kelley, 2011; Flowers et al., 2009; Green & Duddy, 2006; Johnson et al., 2017; Green et al., 2018).

4. Samples and Methods

Mineral separates from 15 samples from the Pilbara Craton and adjacent terranes housed in the University of Melbourne thermochronology group mineral collection were used in this study (Table 1 and Figure 3). Some of the samples used here were previously analyzed in studies using a range of different dating methods: zircon U-Pb and whole rock-minerals Rb/Sr (Oversby, 1976); titanite and apatite fission track (Ferguson, 1981); and AFT, muscovite, and K-feldpar ^{40}Ar/^{39}Ar (Weber, 2002). Analytical methods used in this work are described briefly below.

4.1. AFT Analysis

Apatite grain mounts were polished and analyses performed on image sets captured by TrackWorks using a 3.2MP AVT Oscar F-320C camera mounted on a Zeiss AxioImager microscope with a 1,000X total magnification and a 100X dry objective. Spontaneous track densities were measured on prismatic internal apatite surfaces after etching with 5N HNO_3 for 20 s at 20°C (Gleadow & Lovering, 1978). Track counts were obtained by automated counting in FastTracks using the “coincidence mapping” technique followed by manual inspection (Gleadow et al., 2009, 2015). Uranium concentrations of each grain were determined by LA-ICP-MS single spot analysis using a New Wave Nd:YAG Laser ($\lambda = 213$ nm with 5 Hz @ 45% power, spot size = 30 μm) connected to an Agilent 7700 mass spectrometer. NIST612 was used as primary reference material and a sintered Mud Tank Carbonatite apatite as in-house secondary reference material during LA-ICP-MS analysis. Results were reduced using the software package Iolite (Paton et al., 2011). Single grain and pooled ages were calculated according to Hasebe et al. (2004). Central ages as well as age dispersion and chi-square values were calculated using RadialPlotter (Vermeesch, 2009). All ages are “model” ages obtained using a range factor (R_s) of 7.17 μm (half the average mean track length of Durango apatite) and are directly comparable to conventional External Detector Method ages (Seiler et al., 2014). Confined track lengths (TINTs) were measured as true 3-D lengths using FastTracks and are corrected for a refractive index of 1.634 for apatite.

4.2. (U-Th)/He Analysis

Analysis followed the protocol of House et al. (2000) for laser ^{4}He extraction from single grains for both apatite and zircon. Handpicked, apatite and zircon grains (minimum width of ~75 μm), previously screened for possible microinclusions were imaged microscopically and their dimensions measured using the software ImageJ. They were then placed in small acid-treated platinum capsules and outgassed under vacuum at ~900°C for 5 min (apatite) and ~1,300°C for 20 min (zircon) using a semiconductor Coherent Quattro FAP 820 nm diode laser with fiber-optic coupling to the sample chamber (to provide optimal coupling with samples and heating without melting, ablation, or fusion). He volume was determined by isotope dilution using a pure ^{3}He spike, calibrated against an independent ^{4}He standard, and measured using a Balzers quadrupole (QMS 200-Prisma) mass spectrometer. A hot blank was run after each gas extraction to verify complete outgassing of the apatite grains, and in cases where samples yielded a second re-extract, it contributed <0.5% of the total measured ^{4}He for all samples. Outgassed apatite grains were removed from the laser chamber, dissolved in HNO_3 (still in their Pt capsules), and analyzed for parent isotopes ^{238}U, ^{235}U, ^{232}Th, and ^{147}Sm by external calibration (see below) using an Agilent 7700X inductively coupled plasma mass spectrometer (ICP-MS). Zircon grains, however, were removed from their Pt capsules and transferred to Parr bombs where they were spiked with ^{233}U and ^{229}Th and digested in small volumes of HF and HNO_3 (0.3–0.5 ml) at 240°C for 40 hr. Standard solutions containing the same spike amounts as samples were treated identically, as were a series of unspiked reagent blanks. A second bombing in HCl for 12 hr at 180°C ensured dissolution of fluoride salts. Zircon solutions were then dried down on a hot plate at 145°C for 5–6 hr and then dissolved in HNO_3 and diluted in H_2O to 5% acidity for analysis of ^{238}U, ^{235}U, and ^{232}Th by solution ICP-Mass Spectrometry also using an Agilent 7700X.

Table 1
Sample Details and Summary of Low-Temperature Thermochronology Methods Used

Sample No.	Lithology	Longitude °E	Latitude °S	Elevation (m)	Previous age determinations on sample[a]				Analyses carried out in this study[a]		
					ZrU-Pb	Ar	TiFT	AFT	ZrHe	AFT	AHe
Pilbara Craton (Archean)											
8010-25[b]	Granite	117.62668	−20.71432	n/a					✓	✓	✓
7315-12[c]	Migmatite	119.17750	−21.75060	n/a	✓		✓	✓			
7315-18[c]	Gneissic granite	119.41667	−21.53333	n/a	✓		✓	✓	✓	✓	✓
7315-35[c]	Foliated granite	119.00320	−21.98690	n/a	✓		✓	✓	✓		
7315-41[c]	Granite	118.91650	−21.28890	n/a	✓		✓	✓	✓	✓	✓
0705-03[d]	Granite	116.85758	−20.77253	18						✓	✓
0705-12[d]	Microgabbro	116.83803	−21.09561	80						✓	
0705-19[d]	Gabbronorite	116.85472	−21.14119	103						✓	✓
UW98-27[e]	Granodiorite	118.04778	−20.96889	80						✓	✓
UW98-28[e]	Granodiorite	118.96833	−20.38861	70						✓	✓
UW98-29[e]	Granite	119.68722	−20.35000	90						✓	✓
UW98-34[e]	Granite	119.95361	−21.63333	340							✓
Gascoyne Complex (Proterozoic)											
UW98-23[e]	Syenite	115.47667	−22.58111	110		✓				✓	✓
Hamersley Basin (Proterozoic)											
UW98-17[e]	Granodiorite	117.35722	−22.81194	380						✓	✓
UW98-41[e]	Sandstone	119.08056	−23.52778	640						✓	✓

[a] Analytical method—Zr = zircon U/Pb; Ar = muscovite and K-feldpar Ar/Ar; TiFT and AFT = titanite and apatite fission track, respectively; ZrHe = zircon (U-Th)/He; AHe = apatite (U-Th-Sm)/He. Source of samples (and previous ages reported) from within the University of Melbourne thermochronology group mineral collection. [b] Pilbara excursion—second Archean conference. [c] Oversby (1976) (Ferguson, 1981 = FT ages). [d] Kohn collection, 2005. [e] Weber (2002).

Analyses for parent isotopes were calibrated using the international rock standard BCR-2, and a Mud Tank carbonatite solution (for apatite), and international rock standards BCR-2 and BHVO-2 (for zircons). Raw AHe ages were corrected for α-ejection and the age calculated using the approach of Farley et al. (1996), while for ZHe data the correction prior to age calculation followed the approach of Hourigan et al. (2005). Analytical uncertainties for the Melbourne He facility are conservatively assessed to be ~6.2%, including the α-ejection correction, an estimated 5 μm uncertainty in grain dimensions, gas analysis (estimated as <1%), and ICP-MS analytical uncertainties. Accuracy and precision of U, Th, and Sm parent isotope content ranges up to 2% but is typically better than 1%. Durango apatite (McDowell et al., 2005, AHe reference age = 31.02 ± 1.01 Ma), and Fish Canyon Tuff zircon (Gleadow et al., 2015, ZHe reference age = 28.3 ± 0.4 Ma) were also run as "unknowns" with each batch of apatite or zircons samples and served as an internal check on analytical accuracy (see Tables 3 and 4, respectively).

5. Results

5.1. Apatite Fission Track (AFT)

AFT data for 12 samples are summarized in Table 2, with individual grain age and track length data, together with track length histograms and radial plots presented in Table S1. Pooled and central ages are indistinguishable within analytical uncertainties and range from ~282–427 Ma, with confined mean track lengths (MTLs) falling within a relatively restricted range of 12.78–13.37 μm. Ten of the AFT ages (weighted mean ~373 Ma) across the study area mostly overlap (at ± 2σ) including sample UW98-23 in the Gascoyne Province (Figure 3) with a large uncertainty. However, Samples UW98-28 and UW98-29 at the northern margin of the Pilbara (Figure 1) are markedly younger (weighted mean ~287 Ma), but their MTL fall within a similar range to the other samples. Track-length distributions are unimodal and usually moderately broad, with standard deviations of 1.06–1.71 μm (see Table S1). AFT central ages of 324 ± 18 Ma (Sample 7315-18) and 371 ± 18 Ma (Sample 7315-41) are concordant (at ± 2σ) with previous AFT ages reported for these samples of 331 ± 8 and 328 ± 7 Ma, respectively (Ferguson, 1981). AFT ages reported by Ferguson (1981) on two additional samples (7315-12 and 7315-35), for which we have not determined AFT ages, were 291 ± 7 and 340 ± 8 Ma, respectively. However, AFT ages determined by Weber (2002) for our samples prefixed by

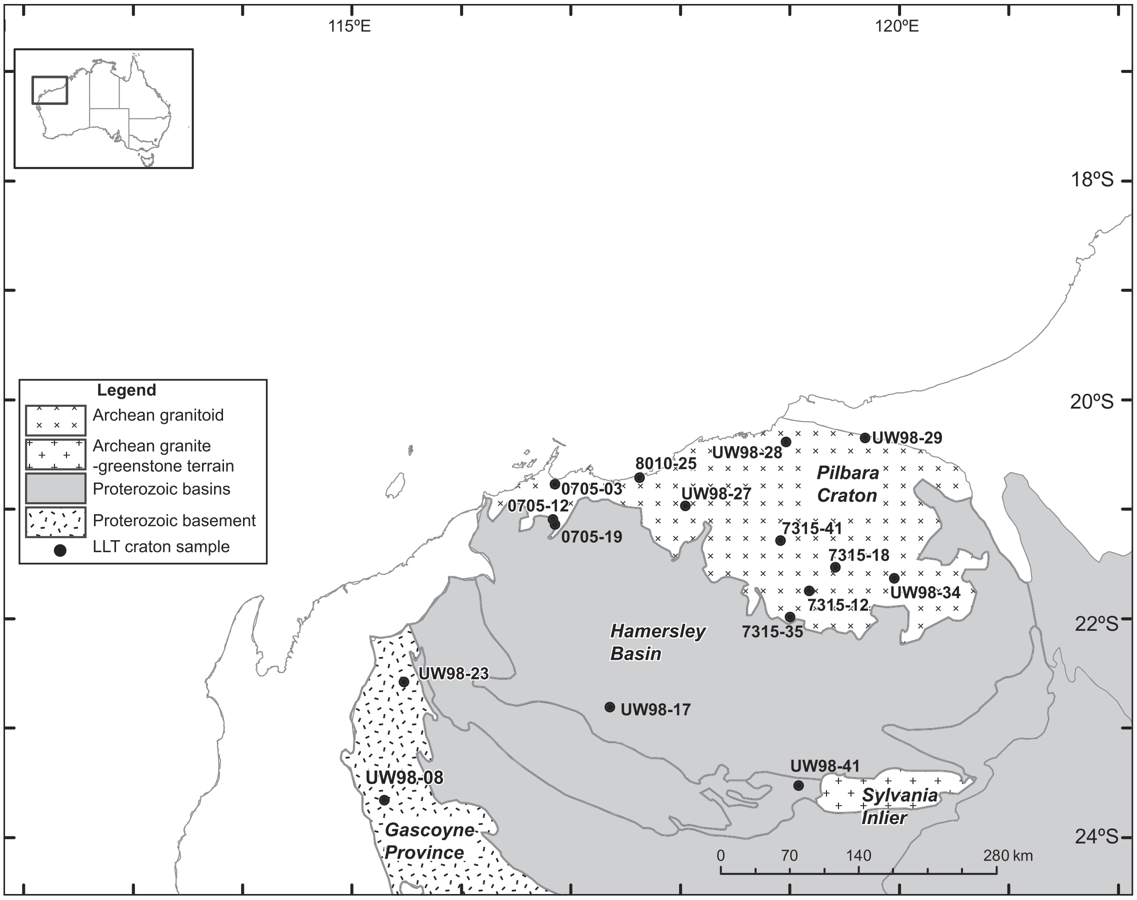

Figure 3. Simplified geological units of the Pilbara Craton and adjacent terranes showing sample localities from which low-temperature thermochronology data were generated for this study.

UW98 from the Pilbara Craton range from 218 to 283 Ma and are consistently younger than those reported here or by Ferguson (1981).

The intrasample AFT grain age dispersion is generally low to moderate (≤21%) for all samples, except for Sample UW98-23 (33%), the youngest recorded in our data set, for which only eight suitable grains were available for age determination (Table 2). Five samples fail the χ^2 test at <5%, seemingly suggesting that the grains counted for these ages are unlikely to be drawn from the same Poissonian distribution and that the sample may contain more than one age population. However, such failure may be expected in slowly cooled basement rocks due to the range of possible kinetic responses to annealing under such thermal history conditions (Galbraith & Laslett, 1993). Apatite grain Dpar values mostly fall between 1.43 to 1.89 μm and do not show any clear relationship with AFT age (Figure 4a). However, Sample 0705-12 (a microgabbro), with the highest mean value of 3.12 μm, shows a moderately positive trend suggesting that the intrasample age variation in this sample is compositionally dependent (Figure 4a).

5.2. (U-Th-Sm)/He

AHe ages for 56 single grains from 12 samples are listed in Table 3 and range from 143 ± 9 Ma to 616 ± 38 Ma. Most samples show some age dispersion patterns similar to those previously reported from other slowly cooled terranes (e.g., Fitzgerald et al., 2006; Flowers, 2009; Flowers & Kelley, 2011; Flowers et al., 2007; Kohn et al., 2009; Mackintosh et al., 2017). ZHe data for 30 grains analyzed from four samples are presented in Table 4. Ages range from 30 ± 2 Ma to 447 ± 28 Ma, with three samples showing considerable intrasample age dispersion, whereas a fourth sample 7315-18 presents a much tighter data set.

Table 2
Pilbara Craton Apatite Fission Track Data

Sample No.	No. of grains	N_s	ρ_s [10^5 cm^{-2}]	^{238}U [ppm]	Dispersion %	P(χ^2) %	Pooled age [Ma ± 1σ]	Central age [Ma ± 1σ]	N_L	Mean track length [µm ± SE]	SD [µm]	*c* axis corrected mean track length [µm ± SE]	Mean Dpar [µm]
8010-25	19	1,987	62.8167	36.82	0.0	60	387.3 ± 11.8	385.4 ± 11.8	93	13.13 ± 0.12	1.15	14.14 ± 0.09	1.43
7315-18	21	2,169	41.3182	28.60	21.0	0	319.1 ± 18.0	323.8 ± 17.6	97	13.21 ± 0.11	1.12	14.18 ± 0.08	1.60
7315-41	17	2,382	51.1258	33.14	15.0	0	369.3 ± 18.9	370.5 ± 17.6	84	13.22 ± 0.12	1.06	14.15 ± 0.08	1.59
0705-03	20	590	7.4967	3.67	0.0	98	422.2 ± 17.0	426.9 ± 25.4	79	12.78 ± 0.17	1.48	13.90 ± 0.12	1.66
0705-12	14	1,543	124.5379	89.01	14.0	1	361.2 ± 19.7	355.2 ± 19.0	23	13.37 ± 0.36	1.71	14.52 ± 0.22	3.12
0705-19	15	728	25.8752	14.48	16.0	2	393.5 ± 28.2	408.8 ± 26.3	48	13.07 ± 0.22	1.49	13.99 ± 0.19	1.87
UW98-17	13	682	28.1663	14.90	11.0	16	410.3 ± 27.0	415.6 ± 25.0	63	12.82 ± 0.15	1.23	13.90 ± 0.12	1.47
UW98-23	8	536	22.8406	15.04	33.0	0	296.7 ± 45.5	282.3 ± 40.0	36	12.82 ± 0.23	1.40	13.64 ± 0.18	1.45
UW98-27	15	2,445	68.3266	41.25	3.3	34	361.3 ± 13.7	361.6 ± 13.1	96	13.40 ± 0.12	1.19	14.33 ± 0.09	1.89
UW98-28	15	1,002	28.8462	19.78	5.5	28	307.7 ± 16.5	313.7 ± 14.5	90	13.10 ± 0.14	1.32	14.11 ± 0.10	1.76
UW98-29	19	2,875	64.7046	48.81	5.5	29	278.0 ± 10.5	283.6 ± 9.9	98	13.08 ± 0.11	1.11	14.11 ± 0.08	1.61
UW98-41	23	2,033	39.3730	23.37	7.2	20	368.5 ± 14.2	364.7 ± 13.6	97	13.08 ± 0.17	1.66	14.10 ± 0.11	1.69

Note. N_s = number of spontaneous tracks counted; ρ_s = spontaneous track density; P(χ^2) = probability obtaining chi-square value for n degree of freedom (where n = No. crystals-1); NL = number of lengths measured; SE = standard error; SD = standard deviation of track length distribution; Dpar = the long axis of a track etch pit parallel to the crystallographic *c* axis is used as a compositional proxy (e.g., Burtner et al., 1994).

5.3. Interpretation of Data Patterns

AFT results are summarized in a boomerang plot (Figure 4b), which is a useful way of displaying graphically the relationship between measured MTL and AFT ages in a sample set (e.g., Green, 1986). For comparison, the range of AHe and ZHe ages are also shown on the plot, with many of the former overlapping or older than the AFT ages, but the latter mostly yielding younger ages. A boomerang plot, indicated by a concave-up pattern, can be used to discern partially thermally reset or nonreset samples lying within or above a paleo-PAZ and estimate the time of onset of the most recent cooling event (Gallagher & Brown, 1997). Nine of the AFT samples are considered to form the ascending arm (left-hand side) of a boomerang (Figure 4b) signifying the cooling of samples from higher temperatures following annealing during residence in the PAZ, with MTL lengthening (although within a somewhat limited range). The timing of the most recent cooling event is constrained by the transition of samples with FT ages and MTL in the 12.5–13.5 µm range to samples as suggested by our data, to younger ages and longer MTL, which have cooled from higher paleotemperatures (e.g., Brown et al., 1994; Gallagher & Brown, 1997). The observed trend of most of our samples suggests that the timing of this transition is mid-Paleozoic in age. Sample UW98-23 is a young age outlier to this trend but only yielded eight grain ages (with large uncertainties) and 36 length measurements, so is not considered to be statistically robust (Figure 4b). Samples UW98-28 and UW98-29, as indicated earlier, yield younger ages and appear to fall off the main trend. This probably indicates that these samples, located at the northern Pilbara craton margin, cooled later from the PAZ compared to those samples forming part of an ascending boomerang arm.

In a detailed study on Canadian Precambrian basement McDannell et al. (2019) revisited the question of REA and concluded that in slowly cooled settings the effects of radiation damage on AFT samples should be considered during thermal history modeling and interpretation. They recommended that at least 35–40 grains be counted if possible and that detailed elemental data be collected for grains on which age and lengths were measured. In terms of such recommendations, our present data set is not sufficiently complete to evaluate this possibility at that level. However, we are able make a first-order assessment as a function of the traditional plots for AFT age or MTL versus eU for all samples (Figures 5a and 5b). For the former plot the relationship between the variables is very weak. The MTL versus eU plot shows a moderate relationship, which is positive and counterintuitive to expectations for the influence of a REA scenario. Taking the AFT data set to a more detailed evaluation we present plots of AFT age versus eU and Dpar versus 3-D track lengths for individual intrasample grains based on data listed in Table S1 and Figure S1. The intrasample single grain data plots all yield very weak to nonexistent relationships between the variables tested. While acknowledging that our data set may not be comprehensive in all parameters, the intrasample data do cover a broad range of eU content and AFT ages, and no clear relationships are apparent, which could be used to further interrogate the thermal history outcomes outlined in section 6.

Table 3
Pilbara Craton Single Grain Apatite (U-Th-Sm)/He Data

Sample No.	Analysis No.	He#	^{4}He (ncc)	Mass (mg)	Mean F_T[a]	U ppm	Th ppm	Sm ppm	Th/U	[eU] ppm[b]	Uncorrected age (Ma ±1 σ)	Corrected age (Ma ±1 σ)	Grain length (μm)	Grain half-width (μm)	R_s[c]	Grain morphology[d]
8010-25	18,043	59,900	5.041	0.0036	0.69	17.9	46.5	332.1	2.60	28.8	380 ± 24	**551 ± 34**	218.5	40.7	51.4	0T[f]
8010-25	18,044	59,903	2.325	0.0023	0.67	21.9	26.2	431.9	1.20	28.1	286 ± 18	**428 ± 27**	201.8	39.6	49.6	1T[f]
8010-25	18,045	59,906	8.428	0.0047	0.72	40.7	17.9	309.0	0.44	44.9	315 ± 20	**437 ± 27**	281.6	40.8	53.5	0T[f]
8010-25	18,046	59,909	6.018	0.0024	0.70	42.0	14.1	367.0	0.34	45.3	431 ± 27	**619 ± 38**	192.3	42.0	51.7	1T[f]
8010-25	18,047	59,912	3.080	0.0022	0.68	27.5	14.9	552.2	0.54	31.0	349 ± 22	**517 ± 32**	196.8	39.5	49.4	1T[f]
Weighted mean: 492 ± 95 Ma, 15% SD[e]																
7315-18	17,844	59,466	10.709	0.0108	0.82	25.7	15.1	111.6	0.59	29.2	271 ± 17	**330 ± 20**	277.3	75.7	89.2	1T[f]
7315-18	17,845	59,469	10.425	0.0134	0.82	20.0	9.2	65.6	0.46	22.2	281 ± 17	**343 ± 21**	287.6	68.0	82.5	0T
7315-18	17,847	59,475	4.172	0.0075	0.77	15.5	8.2	63.5	0.53	17.4	255 ± 16	**333 ± 21**	261.7	58.8	72.0	2T[f]
7315-18	17,848	59,478	9.626	0.0087	0.79	26.3	12.8	84.1	0.49	29.3	302 ± 19	**380 ± 24**	225.0	61.9	72.8	0T
Weighted mean: 344 ± 34 Ma, 18% SD[e]																
7315-41	17,849	59,481	8.130	0.0073	0.78	25.9	22.0	214.4	0.85	31.1	285 ± 18	**366 ± 23**	193.4	61.3	69.8	0T[f]
7315-41	17,851	59,532	12.215	0.0112	0.81	27.4	22.3	272.0	0.81	32.6	265 ± 16	**328 ± 20**	255.7	66.1	78.8	0T[f]
7315-41	17,853	59,538	13.304	0.0105	0.80	29.7	26.1	217.6	0.88	35.8	281 ± 17	**350 ± 22**	236.6	66.6	77.9	0T[f]
7315-41	18,006	59,716	4.441	0.0057	0.76	24.0	23.2	246.2	0.96	29.5	212 ± 13	**279 ± 17**	182.3	55.7	64.0	0T[f]
7315-41	18,007	59,719	4.575	0.0038	0.73	29.9	28.9	281.0	0.97	36.7	262 ± 16	**358 ± 22**	122.1	55.6	57.3	0T[f]
Weighted mean: 328 ± 47 Ma, 10% SD[e]																
0705-03	2,591	6,911	0.511	0.0028	0.67	5.6	6.7	54.3	1.19	7.2	204 ± 13	**303 ± 19**	176.0	39.8	48.7	0T
0705-03	2,593	6,904	0.623	0.0013	0.60	10.8	12.0	110.0	1.11	13.6	280 ± 17	**463 ± 29**	152.0	34.9	42.6	1T
0705-03	2,833	7,560	0.497	0.0021	0.68	3.8	7.0	67.0	1.86	5.4	347 ± 22	**507 ± 31**	137.3	49.0	54.2	1T
Weighted mean: 384 ± 277 Ma, 21% SD[e]																
0705-19	2,856	7,667	2.655	0.0046	0.73	7.2	49.7	101.9	6.95	18.9	245 ± 15	**337 ± 21**	156.9	54.3	60.5	0T[f]
0705-19	2,857	7,670	2.741	0.0040	0.71	8.4	47.6	88.4	5.65	19.6	283 ± 18	**400 ± 25**	157.9	50.0	57.0	0T[f]
0705-19	2,858	7,673	1.146	0.0043	0.72	4.0	29.3	50.2	7.29	10.9	198 ± 12	**274 ± 17**	130.0	57.2	59.6	0T[f]
0705-19	3,085	8,401	1.332	0.0039	0.71	5.0	31.2	72.9	6.26	12.3	223 ± 14	**312 ± 10**	137.5	53.2	57.5	0T[f]
0705-19	3,087	8,395	1.125	0.0034	0.70	4.7	30.4	64.1	6.50	11.8	225 ± 14	**323 ± 20**	140.9	49.1	54.6	0T[f]
Weighted mean: 317 ± 43 Ma, 13% SD[e]																
UW98-17	17,839	59,451	6.743	0.0084	0.76	13.9	17.2	119.3	1.24	17.9	354 ± 22	**466 ± 29**	343.6	49.4	64.8	0T[f]
UW98-17	17,840	59,454	7.254	0.0102	0.78	19.8	24.7	131.5	1.25	25.6	224 ± 14	**287 ± 18**	292.1	64.7	79.5	2T[f]
UW98-17	17,841	59,457	2.895	0.0065	0.76	10.9	11.0	120.7	1.01	13.5	264 ± 16	**350 ± 22**	251.5	50.5	63.1	0T[f]
UW98-17	17,842	59,460	6.253	0.0113	0.80	13.5	16.0	144.1	1.19	17.3	257 ± 16	**320 ± 20**	263.6	65.2	78.4	0T[f]
UW98-17	17,843	59,463	3.380	0.0074	0.77	11.0	11.5	105.0	1.04	13.7	266 ± 17	**346 ± 22**	254.2	53.7	66.5	0T[f]
Weighted mean: 337 ± 71 Ma, 15% SD[e]																
UW98-23	17,814	59,371	0.784	0.0065	0.77	3.0	5.2	53.1	1.75	4.2	226 ± 14	**294 ± 18**	116.9	74.6	68.3	0T
UW98-23	17,815	59,379	1.598	0.0092	0.79	7.9	19.0	74.3	2.40	12.4	113 ± 7	**143 ± 9**	169.5	73.6	77.0	0T
UW98-23	17,816	59,382	2.918	0.0077	0.82	8.5	4.4	61.1	0.52	9.5	316 ± 20	**385 ± 24**	179.8	87.2	88.1	1T
UW98-23	17,817	59,385	1.188	0.0156	0.84	2.7	1.1	31.1	0.41	3.0	207 ± 13	**247 ± 15**	191.0	90.1	91.8	0T
UW98-23	17,818	59,388	1.840	0.0097	0.81	7.0	3.3	76.7	0.46	7.8	195 ± 12	**241 ± 15**	170.9	75.1	78.3	0T

Table 3
Continued

Sample No.	Analysis No.	He#	^{4}He (ncc)	Mass (mg)	Mean F_T[a]	U ppm	Th ppm	Sm ppm	Th/U	[eU] ppm[b]	Uncorrected age (Ma ±1 σ)	Corrected age (Ma ±1 σ)	Grain length (µm)	Grain half-width (µm)	R_s[c]	Grain morphology[d]
Weighted mean: 212 ± 102 Ma, 37% SD[e]																
UW98-27	17,831	59,427	20.063	0.0139	0.79	32.3	76.8	206.1	2.38	50.3	231 ± 14	**292 ± 18**	409.2	58.0	76.2	0T[f]
UW98-27	17,993	59,870	2.752	0.0043	0.74	24.1	67.8	199.9	2.81	40.0	130 ± 8	**175 ± 11**	196.9	56.8	66.1	1T[f]
UW98-27	17,994	59,873	5.957	0.0065	0.75	21.5	54.7	173.5	2.54	34.4	215 ± 13	**285 ± 18**	225.9	53.4	64.8	0T[f]
UW98-27	17,995	59,876	3.705	0.0039	0.72	37.3	71.8	186.8	1.93	54.2	141 ± 9	**197 ± 12**	170.9	47.8	56.0	0T[f]
UW98-27	17,996	59,879	3.478	0.0028	0.66	27.1	93.7	263.5	3.46	49.1	204 ± 13	**307 ± 19**	154.1	46.7	53.7	2T[f]
Weighted mean: 225 ± 75 Ma, 24% SD[e]																
UW98-28	17,824	59,406	19.915	0.0364	0.86	9.4	26.4	110.7	2.81	15.6	281 ± 17	**325 ± 20**	361.2	100.1	117.6	0T[f]
UW98-28	17,826	59,412	8.504	0.0151	0.81	10.1	25.3	50.5	2.51	16.0	283 ± 18	**349 ± 22**	324.9	67.9	84.3	0T[f]
UW98-28	17,827	59,415	60.442	0.0339	0.86	26.1	74.7	148.8	2.86	43.7	326 ± 20	**378 ± 23**	291.2	107.6	117.9	0T[f]
UW98-28	17,828	59,418	7.072	0.0119	0.79	13.4	38.9	62.4	2.91	22.5	213 ± 13	**271 ± 17**	345.4	58.6	75.1	0T[f]
UW98-28	18,001	59,882	3.429	0.0039	0.71	17.3	53.1	145.9	3.06	29.8	235 ± 15	**329 ± 20**	171.8	47.7	56.0	0T[f]
Weighted mean: 323 ± 51 Ma, 11% SD[e]																
UW98-29	17,819	59,391	18.503	0.0151	0.82	33.9	20.1	213.0	0.59	38.6	253 ± 16	**308 ± 18**	301.8	70.5	85.8	0T
UW98-29	17,820	59,394	79.798	0.0111	0.81	241.2	366.5	425.7	1.52	327.3	178 ± 11	**219 ± 14**	285.3	75.2	89.3	1T[f]
UW98-29	17,821	59,397	23.365	0.0101	0.79	37.4	40.1	294.3	1.07	46.8	389 ± 24	**489 ± 30**	264.9	61.7	75.0	0T
UW98-29	17,823	59,403	5.347	0.0046	0.76	29.8	12.7	442.7	0.43	32.8	279 ± 17	**368 ± 23**	223.1	54.4	65.6	1T[f]
UW98-29	17,991	59,867	7.025	0.0049	0.74	20.2	17.5	321.4	0.87	24.3	456 ± 28	**616 ± 38**	208.6	48.4	58.9	0T
Weighted mean: 318 ± 159 Ma, 43% SD[e]																
UW98-34	17,834	59,436	3.460	0.0044	0.73	8.8	21.7	248.1	2.47	13.9	438 ± 37	**604 ± 37**	183.6	49.0	58.0	0T
UW98-34	17,836	59,442	9.296	0.0093	0.78	15.5	25.6	392.7	1.65	21.5	361 ± 22	**465 ± 29**	303.4	55.3	70.2	0T
UW98-34	18,002	59,885	3.392	0.0014	0.63	25.2	113.2	533.5	4.50	51.8	362 ± 23	**578 ± 36**	136.3	39.6	46.1	1T
Weighted mean: 535 ± 192 Ma, 21% SD[e]																
UW98-41	17,809	59,356	3.204	0.0030	0.69	29.4	48.1	356.8	1.63	40.7	210 ± 13	**305 ± 19**	169.3	42.0	50.4	0T[f]
UW98-41	17,810	59,359	3.652	0.0061	0.76	13.4	35.9	310.3	2.68	21.8	218 ± 14	**288 ± 18**	185.4	57.3	65.7	0T[f]
UW98-41	17,811	59,362	3.118	0.0045	0.73	11.7	18.7	117.2	1.61	16.1	342 ± 21	**471 ± 29**	198.5	47.5	57.5	0T[f]
UW98-41	17,812	59,365	5.653	0.0057	0.74	16.2	65.6	114.1	4.04	31.6	252 ± 16	**338 ± 21**	194.7	54.0	63.4	0T[f]
UW98-41	17,813	59,368	2.804	0.0030	0.70	20.7	70.1	449.0	3.39	37.2	198 ± 12	**285 ± 18**	128.0	48.6	52.9	0T[f]
Weighted mean: 302 ± 37 Ma, 23% SD[e]																
Durango	17,980	59,374	17.023	—	1.00	—	—	—	22.26	—	30.4 ± 1.9	**30.4 ± 1.9**	—	—	—	—
Durango	17,982	59,484	4.367	—	1.00	—	—	—	21.78	—	31.8 ± 2.0	**31.8 ± 2.0**	—	—	—	—
Durango	18,015	59,731	13.483	—	1.00	—	—	—	21.70	—	31.8 ± 2.0	**31.8 ± 2.0**	—	—	—	—
Durango	18,060	59,939	3.026	—	1.00	—	—	—	22.62	—	31.7 ± 2.0	**31.7 ± 2.0**	—	—	—	—
Durango	18,061	59,942	8.410	—	1.00	—	—	—	20.19	—	31.7 ± 2.0	**31.7 ± 2.0**	—	—	—	—
Weighted mean: 31.5 ± 0.8 Ma, 1.7% SD[e]																

[a] F_T is the α-ejection correction after Farley et al. (1996). [b] Effective uranium content eU = [U ppm] + 0.235*[Th ppm] (Flowers et al., 2007; Shuster et al., 2006). [c] Equivalent spherical radius ([R_s] = [3*R*L]/[2*[R + L]] after Beucher et al. (2013). [d] Grain morphology—0T = no crystal terminations, 1T = one crystal termination, and 2T = 2 crystal terminations. [e] Weighted mean age ± 95% CI and 1 SD (standard deviation) of corrected ages for all samples. [f] AHe grain that was included in a model/s for sample as presented in Figures 8–10.

Table 4
Single Grain Zircon (U-Th)/He Data

Sample no.	Analysis no.	He#	^{4}He (ncc)	Mass (mg)	^{a}Mean F_T	U ppm	Th ppm	Th/U	^{b}[eU] ppm	Uncorrected age (Ma ± 1σ)	Corrected age (Ma ± 1σ)	Grain length (μm)	Grain half-width (μm)	^{c}Rs	^{d}Grain morphology
8010-25	18038	59789	119.431	0.0076	0.78	595.6	338.5	0.57	675.2	147 ± 9	**188 ± 12**	262.4	45.8	58.5	2T
8010-25	18039	59792	145.985	0.0098	0.77	453.8	145.7	0.32	488.1	190 ± 15	**247 ± 15**	398.1	39.2	53.5	2T
8010-25	18040	59795	85.005	0.0055	0.75	709.1	650.2	0.92	861.9	110 ± 7	**147 ± 9**	250.0	38.9	50.5	2T
8010-25	18041	59798	119.262	0.0057	0.76	987.4	295.8	0.30	1056.9	123 ± 8	**162 ± 10**	239.7	41.1	52.6	2T
8010-25	18042	59801	71.295	0.0082	0.78	680.6	796.9	1.17	867.9	64 ± 4	**82 ± 5**	269.7	46.6	59.6	2T
Weighted mean: 124 ± 70 Ma, 43% SD[e]															
7315-18	17875	59122	149.797	0.0081	0.79	587.1	49.8	0.08	598.8	194 ± 12	**247 ± 15**	285.1	44.6	57.8	2T
7315-18	17876	59125	297.708	0.0094	0.80	985.4	76.9	0.08	1003.5	203 ± 13	**253 ± 16**	284.9	48.6	62.2	2T
7315-18	17877	59128	267.287	0.0154	0.82	594.7	149.5	0.25	629.9	182 ± 11	**221 ± 14**	372.3	53.0	69.6	2T
7315-18	17878	59131	36.403	0.0055	0.75	1073.3	527.5	0.49	1197.3	33 ± 2	**45 ± 3**	246.2	39.6	51.2	2T
7315-18	18033	59774	104.987	0.0088	0.81	951.8	160.0	0.17	989.4	79 ± 5	**98 ± 6**	255.4	51.1	63.8	2T
7315-18	18034	59777	63.176	0.0079	0.78	1183.7	70.2	0.06	1200.2	43 ± 3	**55 ± 3**	274.1	45.0	58.0	2T
7315-18	18035	59780	157.857	0.0116	0.83	934.1	142.8	0.15	967.7	95 ± 6	**115 ± 7**	263.5	59.2	72.6	2T
Weighted mean: 68 ± 44 Ma, 123% SD[e]															
7315-35	17879	59134	182.229	0.0129	0.82	304.3	147.7	0.49	339.0	272 ± 17	**333 ± 21**	290.7	57.9	72.4	2T
7315-35	17880	59137	493.677	0.0323	0.86	237.4	154.4	0.65	273.6	378 ± 23	**440 ± 27**	440.2	72.0	92.8	2T
7315-35	17882	59143	493.616	0.0268	0.86	354.2	289.0	0.82	422.1	299 ± 19	**348 ± 22**	389.5	70.9	90.0	2T
7315-35	17883	59181	121.163	0.0072	0.78	292.5	149.4	0.51	327.6	315 ± 20	**404 ± 25**	252.4	45.8	58.1	2T
7315-35	18036	59783	366.388	0.0189	0.82	304.2	155.1	0.51	340.7	369 ± 23	**447 ± 28**	424.1	54.3	72.2	2T
Weighted mean: 384 ± 65 Ma, 12% SD[e]															
7315-41	17885	59184	120.865	0.0062	0.79	577.4	233.4	0.40	632.2	196 ± 12	**249 ± 15**	214.1	47.9	58.7	2T
7315-41	17886	59187	124.858	0.0106	0.77	627.1	108.9	0.17	652.7	112 ± 7	**146 ± 9**	447.1	38.2	52.7	2T
7315-41	17887	59190	144.028	0.0059	0.78	1759.7	248.0	0.14	1818.0	85 ± 5	**109 ± 7**	225.5	44.5	55.7	2T
7315-41	17888	59193	84.986	0.0059	0.75	393.6	91.6	0.23	415.1	209 ± 13	**280 ± 17**	276.5	37.7	49.7	2T
7315-41	17889	59196	142.327	0.0073	0.80	1049.8	464.1	0.44	1158.9	109 ± 7	**136 ± 8**	208.8	55.5	65.8	2T
7315-41	18025	59750	417.928	0.0111	0.83	1084.7	317.3	0.29	1159.2	216 ± 13	**260 ± 16**	241.9	63.1	75.1	2T
7315-41	18026	59753	214.642	0.0082	0.79	852.5	223.5	0.26	905.0	183 ± 11	**232 ± 14**	273.5	46.3	59.4	2T
7315-41	18027	59756	82.673	0.0089	0.80	734.8	181.9	0.25	777.6	78 ± 5	**98 ± 6**	269.6	49.1	62.3	2T
7315-41	18028	59759	155.175	0.0089	0.80	1202.7	347.2	0.29	1284.3	89 ± 6	**111 ± 7**	238.5	54.9	66.9	2T
7315-41	18029	59762	210.588	0.0175	0.84	1264.4	243.1	0.19	1321.5	63 ± 4	**74 ± 5**	318.7	64.8	80.8	2T
7315-41	18030	59765	165.144	0.0149	0.84	1025.0	454.7	0.44	1131.9	67 ± 4	**80 ± 5**	288.6	64.1	78.7	2T
7315-41	18031	59768	44.528	0.0086	0.80	1342.2	351.8	0.26	1424.9	24 ± 2	**30 ± 2**	258.7	49.8	62.7	2T
7315-41	18032	59771	113.154	0.0062	0.76	648.1	117.9	0.18	675.8	166 ± 10	**218 ± 14**	258.0	40.9	53.0	2T
Weighted mean: 67 ± 34 Ma, 118% SD[e]															
Fish Canyon Tuff															
FCT	17918	59238	8.034	0.0084	0.81	255.5	137.2	0.54	287.8	22.2 ± 1.4	**27.4 ± 1.7**	238.4	52.8	64.8	2T
FCT	18058	59804	5.542	0.0040	0.75	372.2	193.6	0.52	417.7	20.3 ± 1.3	**27.0 ± 1.7**	182.2	42.4	51.6	2T
FCT	18059	59807	7.752	0.0061	0.77	314.5	182.0	0.58	357.3	22.0 ± 1.4	**28.6 ± 1.8**	265.3	39.9	52.0	2T
Weighted mean: 27.6 ± 2.0 Ma, 2.5% SD[e]															

[a] F_T is the a-ejection correction after Farley et al. (1996). [b] Effective uranium content eU = [U ppm] + 0.235*[Th ppm] (Flowers et al., 2007; Shuster et al., 2006). [c] Equivalent spherical radius ([Rs] = [3 * R * L]/[2 * [R + L]]) (Beucher et al., 2013). [d] Grain morphology - 0T = no crystal terminations, 1T = one crystal termination and 2T = 2 crystal terminations. [e] Weighted mean age ± 95% CI and 1 SD (standard deviation) of corrected ages for all samples.

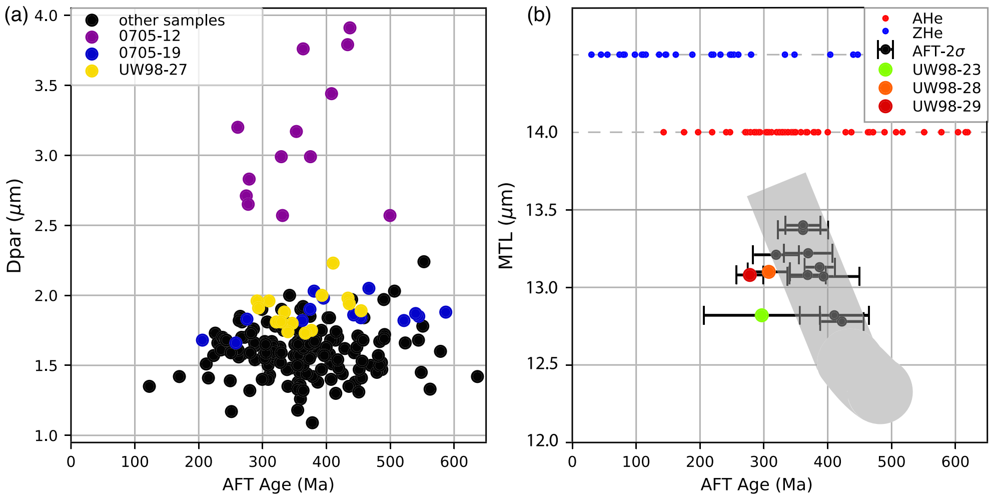

Figure 4. (a) Single grain track-etch parameter Dpar as a function of apatite fission track (AFT) age. Samples with higher Dpar values are color coded and the relationship between the variables as indicated by their trends are weak. If the apparent outlier (at ~500 Ma) for Sample 0705-12 (a microgabbro) is removed then the trend is moderately strong, suggesting that the intrasample age variation in this sample is compositionally dependent. (b) Plot of mean track length (MTL) versus AFT age. MTL are not corrected for *c*-axis orientation (see Table 2). The samples are considered to lie on the left-hand side (ascending limb—characterized by increasing MTL with decreasing age) of a classic "boomerang" trend (shaded area) for most samples, suggesting that the samples record a cooling event (see also section 5.3). Three samples marked in color may plot off this trend. UW98-23 from the Gascoyne Province has a large uncertainty, whereas Samples UW98-28 and UW98-29, located at the northernmost Pilbara craton adjacent to the Canning Basin, are marginally younger and have a different thermal history (see section 6.2.2 and Figure 9). For comparison the range of single grain AHe and ZHe ages are also displayed.

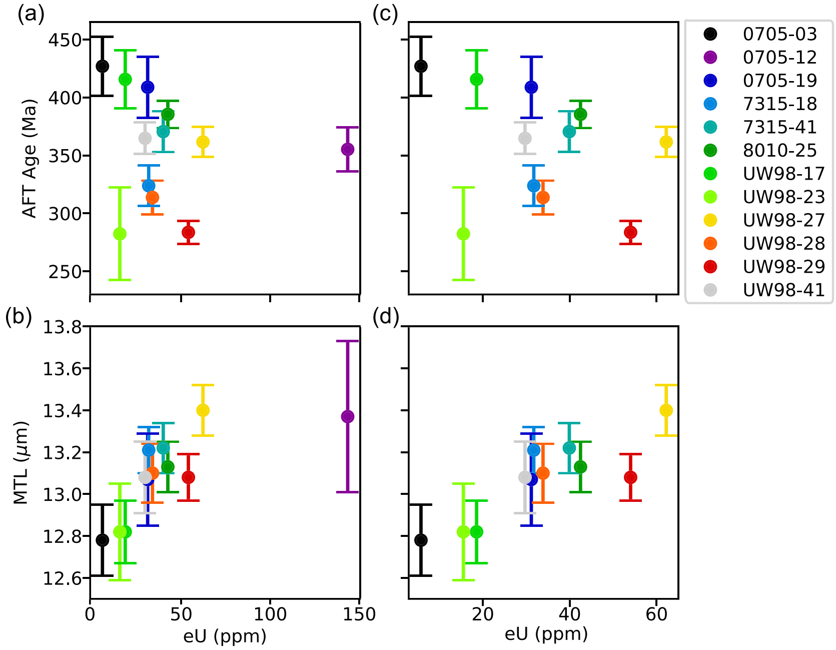

Figure 5. AFT age and mean track length (MTL) versus eU content for all samples (a) and (b), respectively. Note the decrease in age in the former (a) with increasing eU, but increase in MTL for the latter (b). Panels (c) and (d) are plots for the same samples with removal of outlier 0705-12 with a high eU value, but all show weak negative relationship in (c), but a strong positive trend in (d).

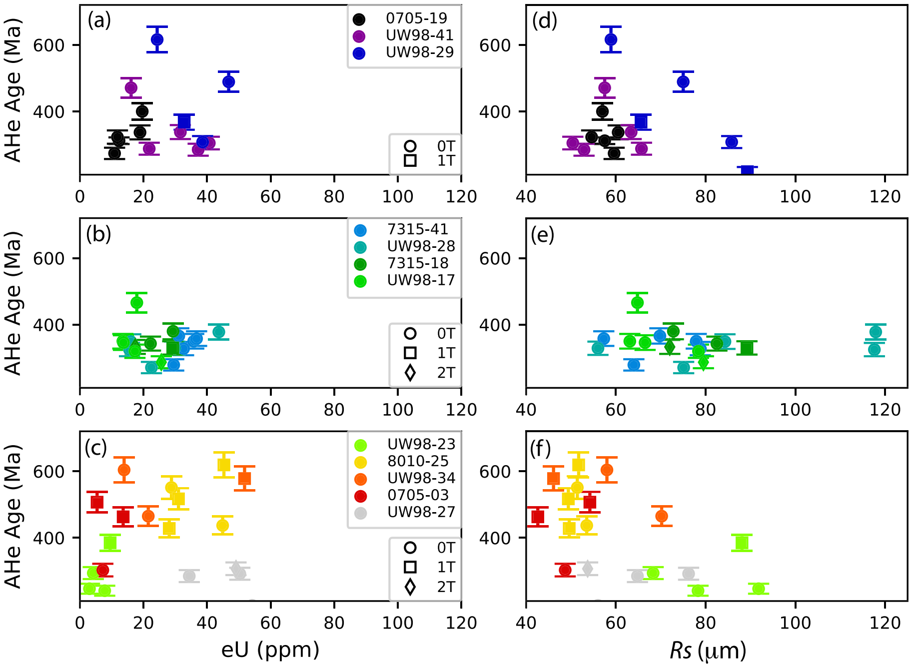

Figure 6. AHe age as a function of effective uranium concentration (eU ppm) (a–c) and equivalent spherical radius (*Rs*) (d–f). AHe ages are plotted with ±1σ uncertainty bars and for each single-grain age, the symbol shape indicates the grain morphology (0T = no terminations; 1T = one termination, 2T = both terminations). See text for further discussion.

As outlined previously, AHe intrasample age data in slowly cooled rocks are often dispersed and may be related to a number of factors, particularly accumulated radiation damage, grain size, and morphology. Laboratory diffusion data suggest that He retentivity in apatite increases with radiation damage and grain size (Shuster et al., 2006), and this may be verified by plots between AHe age or grain size (R_s) versus eU. Plots with these parameters, together with their degrees of fragmentation as recorded by the number of terminations (0T, 1T, or 2T), are shown in Figures 6a and 6b. For the plot AHe age versus eU, only Sample 0705-19 shows a strong positive relationship, followed by Samples UW98-29 and UW98-41 showing moderate negative trends (Figure 6a). In the AHe age versus R_s plot Samples UW98-29, UW98-17, and UW98-34 (Figures 6d–6f) show strong to moderate negative trends. All other samples show weak or no clear trends.

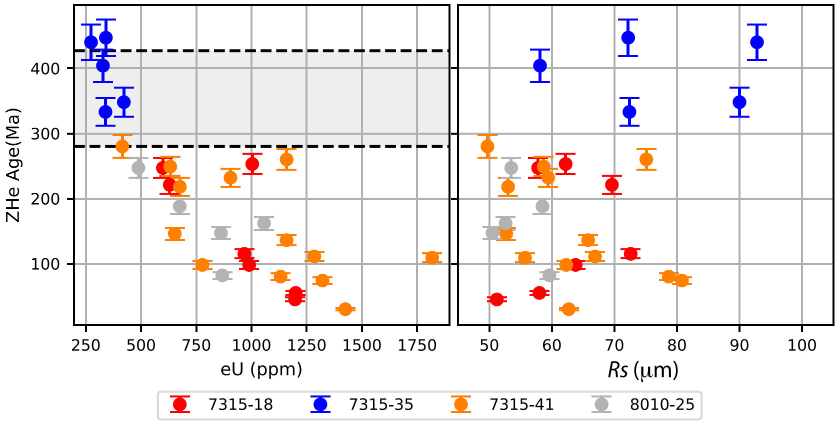

Figure 7. ZHe age as a function of (a) effective uranium concentration (eU ppm) and (b) equivalent spherical radius (*Rs*). ZHe ages plotted with ±1σ uncertainty bars. The gray shaded area bounded by the dashed lines delineates the AFT age range. Note that most ZHe ages are "inverted" with regard to the expected relationship ZHe age >AFT age (see section 3 for further discussion). Trends for samples in plot (b) all show a very weak or no relationship.

Further plots using the same parameters are presented for all intrasample single grains in Figure S2. AHe age dispersion could possibly also be influenced by the fragmentation of grains to varying degrees (see Table 3). Such disruption of the He diffusion profile could result in one termination (1T) fragments yielding older or younger ages than the whole grain age, while no termination (0T) grains would most likely yield older ages (Beucher et al., 2013; Brown et al., 2013). Therefore, variation in degrees of grain fragmentation may mask any possible relationships between AHe ages and eU or grain size (e.g., Wildman et al., 2016); hence, the number of terminations (0T, 1T, or 2T) are recorded in Table 3. The role of other possible factors leading to age dispersion discussed previously is difficult to assess in our samples. He implantation from external sources, such as neighboring grains or thin grain coatings, can be ruled out in most of our samples, which have relatively high eU values (see Tables 3 and S1), with the possible exception of some grains in Samples 0705-03 and UW98-23.

Flowers and Kelley (2011) suggested that highly dispersed sample AHe ages (>20% 1 standard deviation) without age-eU and age-grain size correlations should not be used for thermal history interpretations or that further data should be acquired from those samples. We have listed that data in Table 3, which shows that only six of our 12 AHe samples show standard deviations <20%. Out of all our samples only 0705-19 (Figure 6a) showing a strong positive age-eU relationship and sample UW98-17 (Figure 6e) showing a moderate negative age-grain size trend have standard deviations <20% (Table 3).

ZHe ages are plotted as a function of eU and grain size in Figures 7a and 7b, respectively. Single grains in Sample 7315-35, with the lowest eU values, show a standard deviation <20% and yield the oldest ages observed (between 333 and 447 Ma), whereas grains in the other three samples show wide age dispersion and are negatively related to varying degrees (Table 4 and Figure 7a). No significant trends are evident in the ZHe age versus grain size plot data (Figure 7b). The ZHe age-eU pattern observed is similar to that previously noted in several works (e.g., Boone et al., 2018; Guenthner et al., 2013, 2014; Ketcham et al., 2013; Mackintosh et al., 2017; Orme et al., 2016; Reiners, 2005). Guenthner et al. (2013) demonstrated that the pattern observed results from differences in intragrain He diffusivity related to the degree of accumulated radiation damage. Clearly, this variance can result in a range of intrasample ZHe ages, which will be enhanced by prolonged residence below temperatures of total radiation damage annealing. This may also result in a reversal of the expected relationship ZHe > AFT ages (e.g., Johnson et al., 2017; Mackintosh et al., 2017). While radiation damage is clearly a primary factor controlling age dispersion in our samples, eU zonation may also contribute to some age scatter (e.g., Bargnesi et al., 2016; Danišík et al., 2017; Dobson et al., 2008; Guenthner et al., 2013; Hourigan et al., 2005). The strategy used in this work for obtaining thermal histories for interpreting our data is outlined in section 6 below.

6. Inverse Thermal History Modeling

6.1. Strategy

In this work, inverse thermal history models were produced using the QTQt software (Gallagher, 2012). QTQt uses a Bayesian trans-dimensional Markov Chain Monte Carlo (MCMC) approach to invert low-temperature thermochronology data and produce a series of accepted thermal histories as determined by the data (Gallagher, 2012; Gallagher et al., 2009). Here, we define a time-temperature model space, the present-day surface temperature estimated at 20 ± 10°C, and a constraint for some models indicating that the sample was probably exposed or at least in a near-surface environment at some time during Permo-Carboniferous glaciation as prior probability information (Gallagher, 2012). The MCMC algorithm searches the user-defined time-temperature model space and generates a random model. It then produces a sequence of proposed models that are either accepted or rejected depending on the fit of the modeled data with the observed data relative to the previous model (Gallagher et al., 2009; Wildman et al., 2016).

A detailed account of the modeling approach employed in this study can be found in Mackintosh et al. (2017). Briefly, for all our models, the MCMC sampler was run for 200,000 iterations with the first 50,000 discarded as burn in Gallagher et al. (2009). For each sample a broad initial constraint of 600 ± 100 Ma and a temperature of 70 ± 70°C was used for the general time-temperature prior (model space). Thus, the MCMC algorithm for these initial model runs was able to search the entire general prior time-Temperature (tT) space. We used the QTQt default values for the time range, which represent the oldest single grain age in the sample ± oldest single grain age in the sample. Depending on the sample, this extended the time range of the model space back to between 600–1,200 Ma. However, as illustrated even in the cropped thermal history models shown in Figures 8–10, the thermal history information provided by the AHe, AFT, and ZHe data from the samples in this study is poorly constrained (i.e., the 95% confidence intervals generally span most of the temperature space) prior to ~500 Ma. This was clear from the initial model runs, which showed that the low-temperature thermochronology data could not provide any credible thermal history information prior to that time. The time range, which greatly exceeds the oldest low-temperature thermochronology ages and their uncertainties measured in our samples, was chosen as initial model runs showed that our data could not provide any credible thermal history information prior to that time. For modeling the AFT data, we used single grain age information, together with the annealing model and *c* axis projected confined track length information (Donelick et al., 1999; Ketcham et al., 2007). For AHe data we used the damage-diffusion model of Gautheron et al. (2009) and for ZHe data the zircon radiation damage accumulation and annealing model (ZRDAAM) (e.g., Guenthner et al., 2013).

For all models generated, to ensure confidence in the outputs, only the AFT data were first employed to establish a baseline, from which different model versions could be made progressively. We did not attempt to model AFT Samples UW98-23 and 0705-12 due to few age grains and track lengths being available for measurement, respectively. Because of complexities in (U-Th)/He systematics as outlined in section 5.3, intrasample age dispersion (Tables 3 and 4) and our inability to always account for some of the possible factors involved, less weighting was given to AHe and ZHe data for modeling. As a result, these data were progressively incorporated to AFT models to provide additional constraints. It is in this context that the inverse thermal history modeling software, QTQt, was chosen. With QTQt, AHe and ZHe data can be resampled from their ages, meaning some of the undefined uncertainty can be accounted for by regarding the He ages as less precise while still honoring the observed ages (Gallagher, 2012). Furthermore, it is possible to model AHe data from broken 1T apatite grains using the 1T fragmentation model of Brown et al. (2013) implemented into QTQt. Hence, rather than using averaged AHe data for samples with standard deviation <20%, we chose to model grains based on their morphological characteristics; therefore, AHe grains were not modeled from samples for which there was no coexisting baseline AFT model available. In some cases, however, zero termination (0T) AHe grains were also modeled (Figures 8–10) using the 2T fragmentation model to check whether the effect of fragmentation was sufficiently minor that the diffusion models were still able to successfully replicate the observed AFT data. AHe grain ages used for modeling are marked in Table 3.

Recent studies have highlighted that, with respect to ZHe thermochronometry, there are still unsolved issues in understanding the relationship between radiation damage accumulation and annealing models. This is especially the case in geological environments that have experienced protracted thermal histories within the HePRZ, as would be the case for our samples (e.g., Boone et al., 2018; Ginster et al., 2019; Mackintosh et al., 2017; Reiners et al., 2018). Note also that all zircon grains analyzed in this study were 2T grains, so fragmentation was not an issue for grain selection, and as such, all grains analyzed were incorporated into the relevant models.

6.2. Model Results and Interpretation

Model outputs for 10 samples are presented in Figures 8–10. In these models, the thermal history prior to ~600 ± 100 Ma is poorly constrained, as can be seen from the broad 95% confidence interval, which ranges across much of the temperature space. However, previous higher-temperature geochronological data from some of our samples provide supporting evidence that their low-temperature thermochronology systems were most likely totally reset prior to Paleozoic cooling, suggesting that the initial temperature range used is acceptable for modeling our samples.

In the Pilbara Craton, U-Pb zircon and Rb-Sr age data on some of our samples (Table 1) yield Paleoproterozoic to Archean ages (Oversby, 1976). Further, Sample 7315-18 yielded a titanite fission track age of 1,390 ± 46 Ma (Ferguson, 1981). The effective track retention temperature for this system is ~250°C (e.g., Gleadow & Lovering, 1978). Whereas thermal history modeling of discordant ^{40}Ar/^{39}Ar K-feldspar age spectra from two samples (one very close to our Sample UW98-28) in the eastern Pilbara Craton by Weber (2002) suggest a cooling episode to temperatures of ~175 ± 25°C between ~1,700 and 1,500 Ma. This may be related to post-Capricorn Orogeny (~1,840–1,800 Ma) cooling and/or the Mangaroon Orogeny (1,680–1,620 Ma; Cawood & Korsch, 2008). However, these estimates for lower temperatures in the less sensitive thermal history segments of the models are not considered to be well constrained. In the

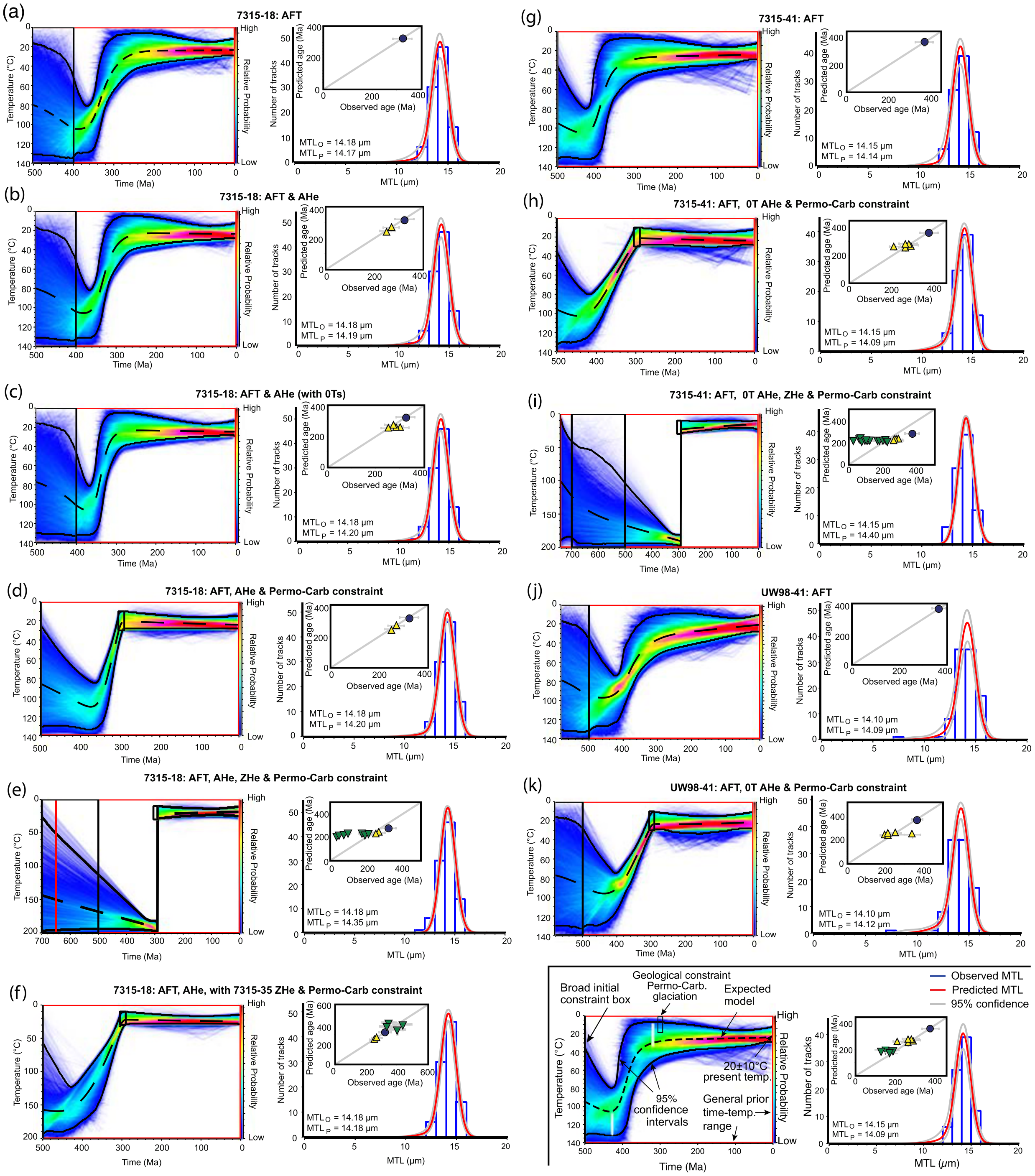

Figure 8. QTQt thermal history inversion color maps based on AFT, AHe, and ZHe data from representative samples in the southern Pilbara Craton and eastern Hamersley Basin showing a pronounced Paleozoic cooling episode commencing between ~420 and 350 Ma (see section 6.2.1 for further discussion). Color map at bottom right corner shows main plot elements. Lower left color maps represent the posterior probability distribution of accepted thermal history models with the dashed line representing the (weighted mean) expected model and the black solid lines representing the 95% confidence intervals. The red box represents the prior time-temperature model space, and the black box represents an additional thermal history constraint used as a starting point for models (see section 6.2). In some cases evidence for parts of the Pilbara Craton having been at the surface or in a near surface environment during Permo-Carboniferous glaciation has been added as an independent geological constraint and for comparison with models where such a constraint was not added. In the bottom right corner map, the right-hand panel showing the histogram represents a comparison of the observed (o) and predicted (p) mean track length (MTL) distribution and values. The red curve represents the predicted track length distribution, and the gray lines indicate the 95% confidence intervals of the predicted distribution. Inset shows the observed corrected ages (with resampled He error values) plotted against the predicted model ages: solid blue circles = AFT ages; yellow triangles = AHe ages; and inverted green triangles = ZHe ages.

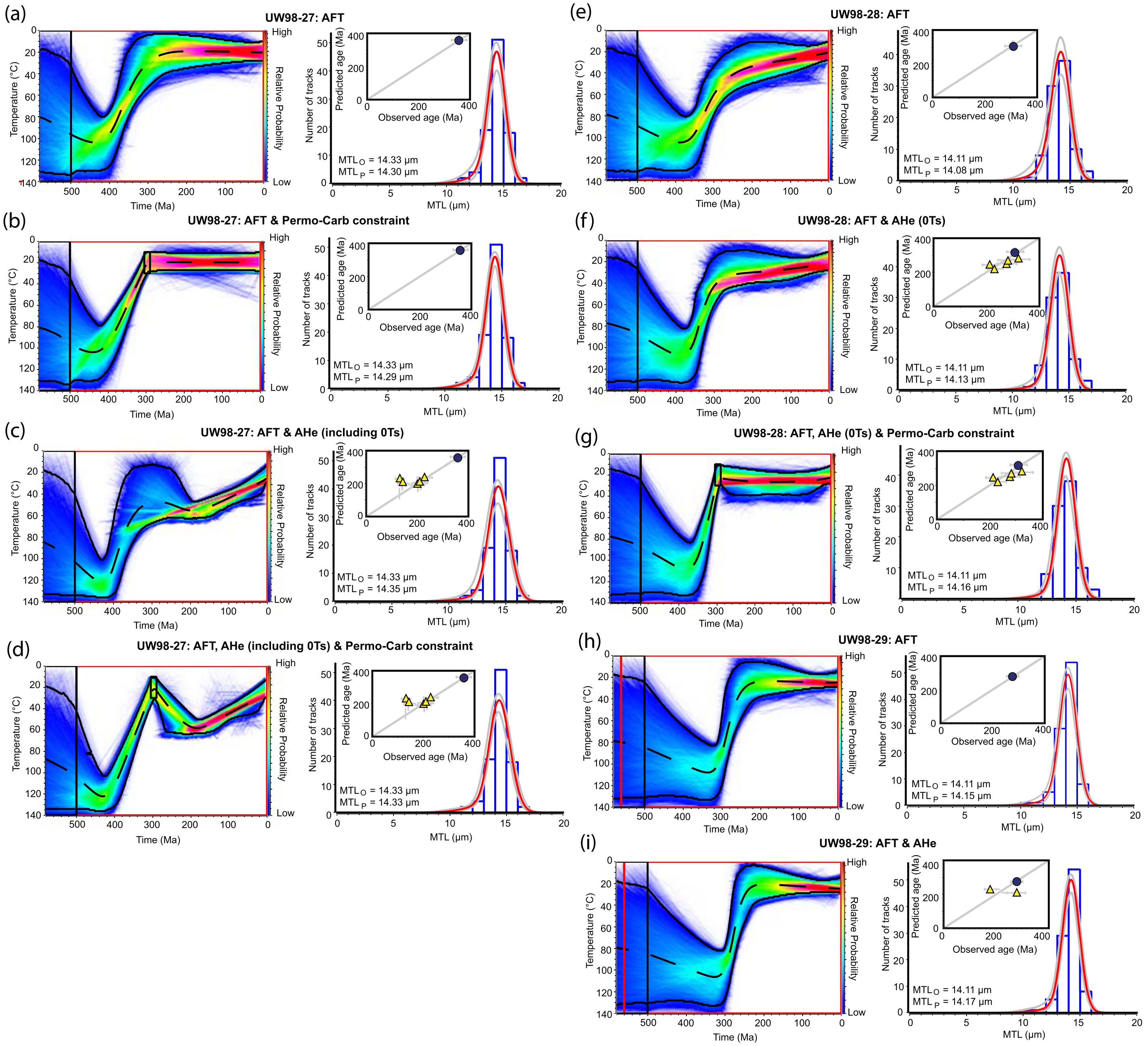

Figure 9. QTQt thermal history inversion color maps based on AFT and AHe data from samples in the central-west and northern Pilbara Craton showing a pronounced Paleozoic cooling episode (see section 6.2.2 for further discussion). Color map elements as for Figure 8.

Gascoyne Complex to the south, a discordant ^{40}Ar/^{39}Ar age spectrum from Sample UW98-23 yields a mean weighted age of 888 ± 5 Ma (muscovite) and 610 ± 1 Ma (K-feldspar), with a minimum age for the latter of 384 ± 1 Ma (Weber, 2002). A further sample from the complex (UW98-08; see Figure 3) yields a mean weighted age of 1,027 ± 1 Ma (muscovite) and 695 ± 1 Ma (K-feldspar), with a minimum age for the latter of 432 ± 1 Ma. Monotonic thermal history models for these samples constructed using Lovera FORTRAN codes (e.g., Quidelleur et al., 1997) indicate a general period of slow cooling between ~1,000 and 450 Ma, during a phase of quiescence in the tectonic evolution of Proterozoic Australia between ~1,000 and 750 Ma (Cawood & Korsch, 2008; Myers et al., 1996). This was followed by an early Paleozoic cooling inflection at ~180°C for UW98-08, but this temperature is lower and less well constrained for

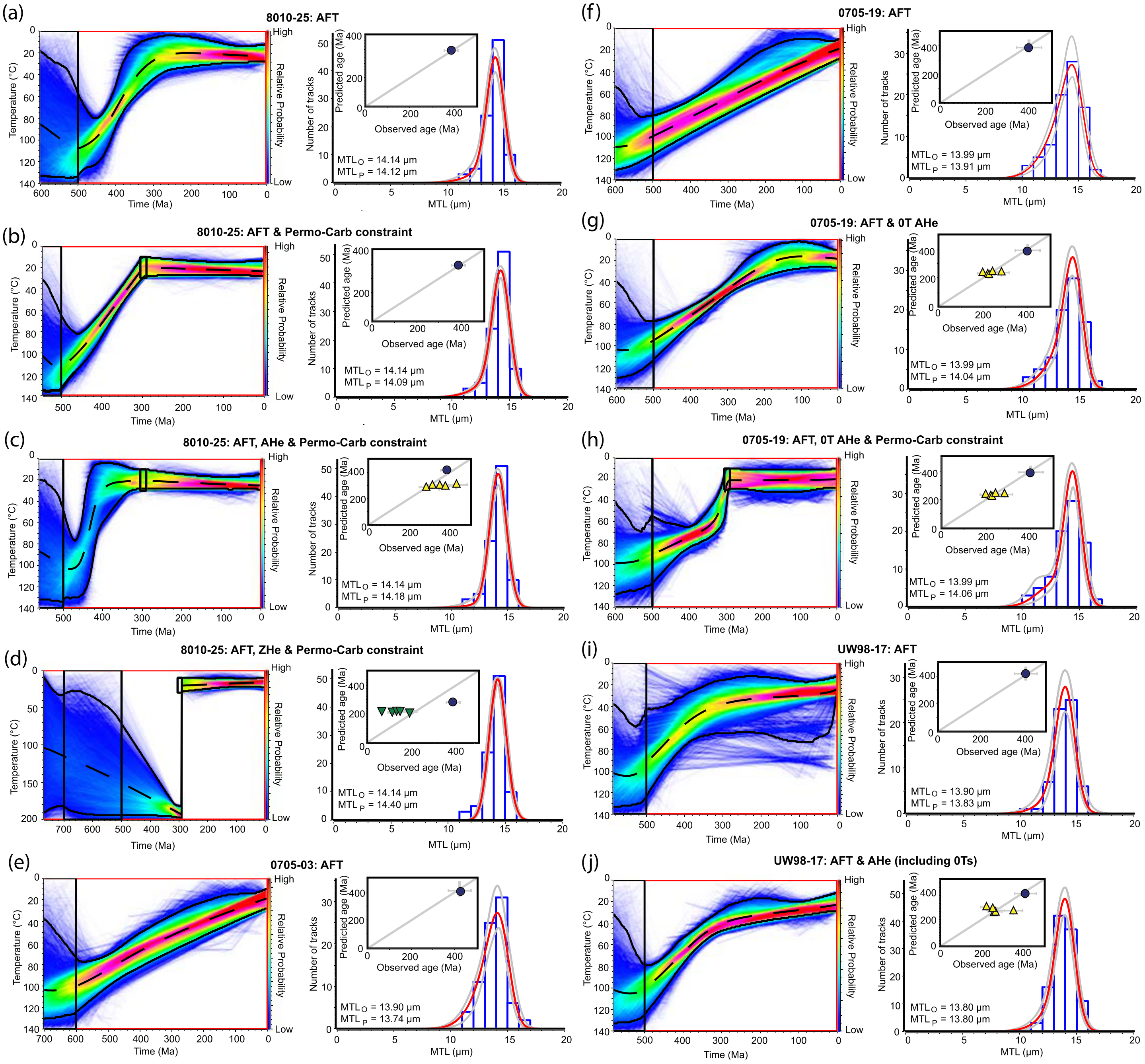

Figure 10. QTQt thermal history inversion color maps based on AFT, AHe, and ZHe data from representative samples in the westernmost Pilbara Craton and central Hamersley Basin episode (see section 6.2.3 for further discussion). Color map elements as for Figure 8.

Sample UW98-23 (Weber, 2002). It is emphasized that at such relatively low temperatures, the K-feldspar thermal history models used are not well constrained since the sensitivity of the models decreases at lower temperatures. Hence, we have not incorporated these data directly into our models.

Based on the cooling patterns observed in the inverse thermal history models (Figures 8–10), it is convenient to divide the models into three areal groupings; *southern Pilbara and eastern Hamersley Basin* (Figure 8), *west-central and northern Pilbara* (Figure 9), and *westernmost Pilbara and central Hamersley Basin* (Figure 10).

6.2.1. Southern Pilbara-Eastern Hamersley Basin

AFT models (Samples 7315-18, 7315-41, and UW98-41) mostly show the onset of a pronounced cooling episode between ~400 and 350 Ma, although eastern Hamersley Basin cooling may have commenced a little earlier (Figures 8a, 8g, and 8j). In all models the onset of cooling was determined by a clear change in trajectory of the expected model path within the 95% confidence interval. Cooling occurred from temperatures of ~100° ± 10°C within the PAZ and typically ranged over ~50–70°C based on our expected models with a ± ~25–35°C uncertainty at the 95% confidence interval. Pronounced cooling continued at an estimated rate of ~1 ± 0.5°C/Ma to ~300 Ma, after which samples resided within a near surface environment through to the present. In Sample 7315-18, the addition of a 1T and 2T AHe grain to our models honor the AFT model (Figure 8b), then the addition of two further 0T AHe grains continues to replicate the AFT data (Figure 8c). The model is then tested with the addition of a constraint reflecting sample exposure at the surface during Permo-Carboniferous glaciation (Figure 8d). This does not significantly change the model, as previous model predictions position the sample in a near surface environment around that time (Figure 8a); however, it does slightly steepen the cooling path trajectory with cooling commencing from ~350 Ma. Figure 8e further builds on that model by adding the sample ZHe data (eU range 599–1,200). The thermal history path is now forced to cool from a temperature of ~190 ± 10°C to the surface at a cooling rate more than 3 orders of magnitude compared to previous models. This is not a credible scenario, and further, all the ZHe ages are mostly overpredicted by utilizing the current ZRDAAM (i.e., they underestimate He retentivity) and are largely incompatible with their coexisting AFT and AHe data. This is also clear in AFT, AHe, and ZHe models where no Permian-Carboniferous glaciation constraint is used and resulting thermal history models are highly improbable (Figures S3a and S3b). Similar observations where ZRDAAM is unable to replicate intrasample ZHe variability have been previously reported (e.g., Boone et al., 2018; Guenthner et al., 2014; Johnson et al., 2017; Mackintosh et al., 2017, 2019); Orme et al., 2016. ZHe grains from Sample 7315-35 display relatively low eU (range 274–422 ppm) and age standard deviation (Table 4), but there is no coexisting AFT data available for this sample for which a baseline thermal history could be established. Therefore, we incorporated these data into a model from nearby Sample 7315-18, which shows a consistent thermal history pattern (Figures 8a–8d). In this case the ZHe data are reproduced well and suggest cooling from ~150 ± 25°C to ~20°C over ~100 Ma (Figure 8f). Models for Samples 7315-41 and UW98-41 (eastern Hamersley Basin) show similar thermal history paths (Figures 8g, 8h, 8j, and 8k) to Sample 7315-18. Further, the ZHe ages in Sample 7315-41 once again largely overpredict the observed ages and are inconsistent with the intrasample variability.

6.2.2. West-Central and Northern Pilbara

AFT data-only models for Sample UW98-27 (west central Pilbara) with and without a Permo-Carboniferous constraint are very similar to those described in section 6.2.1 above (Figures 9a and 9b). However, when AHe data with a range of morphologies are added to the model, some of the AHe grains overpredict ages, leading to an apparent episode of Permo-Triassic heating (Figures 9c and 9d). These models are not considered robust, so in this case we prefer the AFT only models, which more closely follow those to the east. The NW Pilbara models for Samples UW98-28 and UW98-29 are characterized by a later onset for Paleozoic cooling between ~350 and 300 Ma from temperatures within the PAZ (Figures 9e and 9h), and models resulting from the addition of AHe data in both cases are compatible with the AFT only models (Figures 9f and 9i), but more so for UW98-28. However, a Permo-Carboniferous constraint can only be incorporated for Sample UW98-28 (Figure 9g) as models for Sample UW98-29 indicate that it cooled later and only attained residence in a near surface environment in post-Permo-Carboniferous glaciation time.

6.2.3. Westernmost Pilbara and Central Hamersley Basin

AFT data-only models for all samples in this group are characterized by an earlier timing for onset of cooling at between ~500 and 600 Ma compared to other groups. Sample 8010-25 suggests that it had cooled to near surface conditions by the time of Permo-Carboniferous glaciation (Figures 10a and 10b). The addition of AHe data with a Permo-Carboniferous constraint (Figure 10c) suggests that cooling to surface temperatures occurred between ~450 and 400 Ma, but in this case most of the AHe data are underpredicted, suggesting that it is not a robust model. ZHe age data (eU range 488–1,057) are incorporated into AFT model (Figure 10b). As for models generated in Figure 8 the thermal history path is again forced to cool from a temperature of ~190 ± 10°C to the surface at an improbably high cooling rate. Once again, most of the ZHe ages are overpredicted by the ZRDAAM even though grains have a moderate eU range. This is also clear in an AFT, AHe, and ZHe model for Sample 8010-25 where no Permian-Carboniferous glaciation constraint is used and the resulting thermal history model is highly improbable (Figure S3c). AFT models for Samples 0705-03 and 0705-19 show simple linear cooling histories (Figures 10e and 10f), suggesting very slow cooling rates. As both samples have a reasonable number of grain ages measured and track lengths measured, with one passing and the other failing the chi-square test at >5% (Table 2), there is no obvious reason for this result. However, AHe age data incorporated into the AFT model for 0705-19 is compatible with a slow cooling scenario (Figure 10g). The addition of a Permo-Carboniferous constraint in this model forces a rapid cooling event at ~300 Ma from a temperature of ~60°C (Figure 10h). Such a scenario has not been recorded in any other samples in the study area and suggests that such a constraint is not appropriate for this sample. The AFT model for Sample UW98-17 from the Hamersley Basin also suggests a slow cooling scenario (Figure 10i), which is also generally supported by the addition of three of four AHe ages (Figure 10j).

7. Discussion

7.1. Paleozoic Cooling

Thermal history modeling based on AFT data in combination with different variations of AHe and ZHe data reveals a regionally extensive Paleozoic cooling episode spanning most of the Pilbara craton. Cooling in the central and southeastern Pilbara, and eastern Hamersley Basin commenced at ~420 to 350 Ma, whereas in the NW Pilbara, it commenced later ~350–300 Ma. Most of this cooling was completed by ~300 Ma and is supported by independent evidence for Permo-Carboniferous glaciation recorded at this time in some parts of Pilbara bedrock. Samples in the westernmost Pilbara and central Hamersley Basin mainly record a slow cooling pattern, which appears to have commenced between ~500 and 600 Ma and continued at a slow rate through to the present day. Following Paleozoic cooling, samples resided in a near surface environment through to the present day. We interpret Paleozoic cooling as a significant denudational event and suggest that the unroofed and denuded sediments were deposited in the adjacent Canning Basin (Figure 1) in accord with the basin's infilling history (Figure 2; Hashimoto et al., 2018; Romine et al., 1994; Shaw et al., 1995). Although, some Canning Basin infill also had contributions from far-field sediment sources (Haines et al., 2013; Morón et al., 2019). The lack of detrital zircons of Archean age in the Paleozoic sedimentary units of the Canning Basin (Haines et al., 2013; Morón et al., 2019), or in Mesozoic strata in the offshore NW Shelf basins (Lewis & Sircombe, 2013; Morón et al., 2019), indicates that despite its proximity, the Pilbara Craton was not a major sedimentary source for these basins. As such, the regional Paleozoic cooling episode recorded by Pilbara Craton samples in this study may suggest that a previously extensive sedimentary cover, now completely eroded, overlay much of the study area prior to the onset of Paleozoic cooling episode identified by our low-temperature thermochronology data.

Similar thermal history patterns observed in cratonic areas elsewhere have also been linked to burial and unroofing of overlying strata, rather than to the removal of large sections of crystalline shield rocks (e.g., Ault et al., 2013; Harman et al., 1998; Kohn, Gleadow, et al., 2002; Veevers et al., 2005). For example, the Perth Basin, located west of the Yilgarn Craton (Figure 1), hosts up to 15 km of Ordovician to Quaternary strata in major depocenters. The sediments show a predominance of Mesoproterozoic detrital U/Pb zircon ages, with relatively few Archean grains (e.g., Cawood & Nemchin, 2000), suggesting that despite its close proximity, the extensive Yilgarn Craton was not an important provenance for basin fill. Furthermore, recent detrital records of river systems and coastal deposits adjacent to shields do not contain the expected significant zircon populations given their close location to exposed cratonic areas (e.g., Western Australia Quaternary coastal deposits, Sircombe & Freeman, 1999; Mississippi River, Blum et al., 2017; Amazon River, Mason et al., 2019). One explanation for this lack of detrital contribution from cratons is that their peneplanation was complete before the Quaternary and that denudation rates have been minimal since that time (Sircombe & Freeman, 1999). A complementary explanation is that this reflects the strong contrast in the strength and erodibility between cratons and their potential covering strata (e.g., Flowers & Ehlers, 2018) or that cratons have a lower erodibility compared with other rocks (Dhuime et al., 2011).

The timing of the cooling episodes recorded in Figures 8 and 9 corresponds with cooling events related to the Late Ordovician-Carboniferous intraplate Alice Springs Orogeny in southcentral Australia (e.g., Glorie

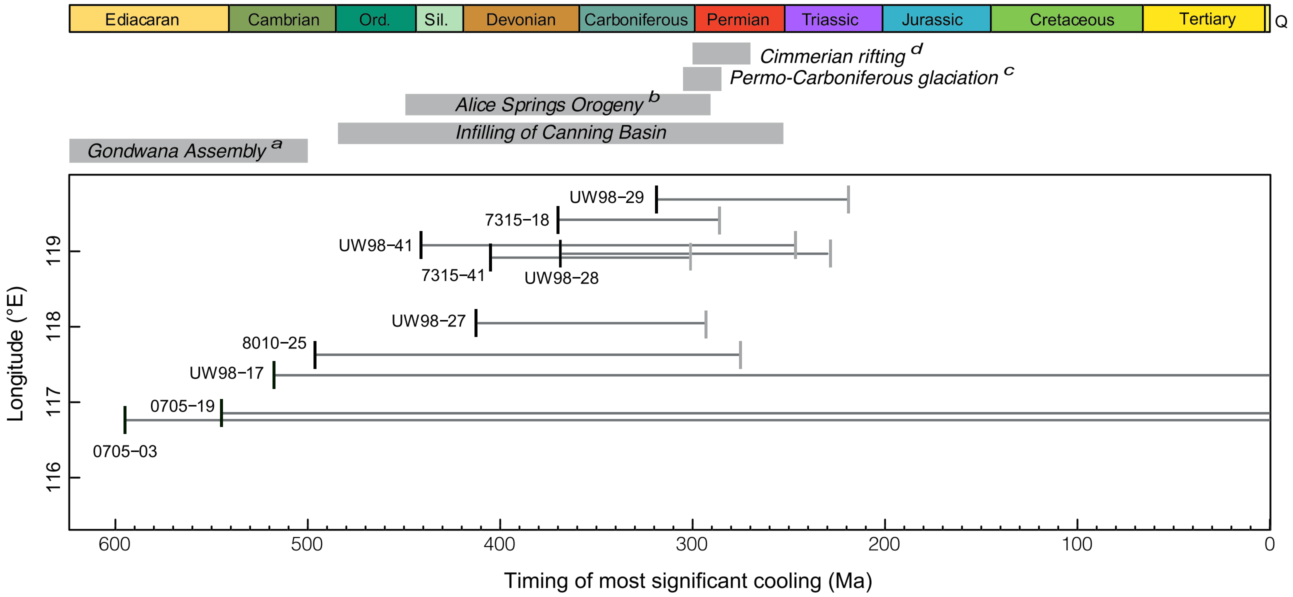

Figure 11. Summary showing longitude of sample locations versus the timing of most significant cooling in the Pilbara Craton and Hamersley Basin based on AFT models (Figures 8–10), and major regional geological events. Note that the approximate timing of cooling onset youngs toward the east and that the age range for most cooling spans ages ~420–290 Ma, which coincides with the duration of the Paleozoic Alice Springs Orogeny, with several samples attaining residence at the surface or in a near surface environment by the time of Permo-Carboniferous glaciation. Timing of major regional geological events is based on the following publications: (a) Haines et al. (2013); (b) Shaw et al. (1991), Collins and Shaw (1995), Buick et al. (2008), and Glorie et al. (2017); (c) Mory et al. (2008); and (d) Yeh and Shellnutt (2016).

et al., 2017) (see Figure 11). Previous numerical modeling may help explain the causal effect of the Alice Springs Orogeny and the opening of the Canning Basin, where we suggest much of the denuded sediments were deposited. Roberts and Houseman (2001) proposed that clockwise rotation of the northern boundary of a lithospheric sheet with an internal weak zone produced crustal thickening in the region representing central Australia, where the Alice Springs Orogeny took place, and thinning in the region representing the Canning Basin. Further, their thin, viscous sheet model provides a mechanism for far-field forces to generate compression and uplift for the Alice Springs Orogeny and extension in the adjacent Canning Basin. Far-field stresses transmitted to cratons over hundreds of kilometers, although related to a different tectonic regime, have also been attributed to deformation in the Canadian Shield (Pinet, 2016). We suggest that lithospheric extension and opening of the Canning Basin may have been linked to a change in base level, which in turn triggered denudation of a sedimentary cover from much of the neighboring Pilbara Craton and eastern Hamersley Basin. This interpretation is also substantiated by the spatial trend of decreasing cooling ages away from the Canning Basin and therefore the rift axis (Figure 11). Such a spatial trend has been observed in other rifts in the Eastern South American and South Western African margins (e.g., Wildman et al., 2019). Furthermore, changes in denudation have been documented in the Quaternary where changes in base level modify topographic gradients, resulting in increased erosion (e.g., Holbrook et al., 2006; Stokes & Mather, 2000). Most of the basin infill in the Canning Basin lacks surficial outcrops, which hinders the ability to obtain paleocurrent data. However, paleocurrent data from exposed Permian sequences suggests that there were secondary sediment transport pathways with an eastward direction flow (Morón et al., 2019; Mory & Haines, 2013). Furthermore, based on along-strike seismic lines (Hashimoto et al., 2018), it can be inferred that some of the sediment transport and basin infill (Figure 2) took place via transverse drainage networks on the rift shoulders, with one of them sourcing sediments from the sedimentary cover overlying the Pilbara Craton.

The timing of other large-scale events, such as the rifting of terranes along the southern Tethys margin related to early stages of the rifting of Pangea (Yeh & Shellnutt, 2016), does not correspond with the cooling ages observed here (Figures 8 and 9). Furthermore, the regionally extensive nature of Phanerozoic cooling detailed here and from other areas of the Western Australian Craton (e.g., Kohn, Gleadow, et al., 2002; Weber et al., 2005) argue against an interpretation that the cooling signal is directly related to a rifting event. However, we note that Paleozoic cooling in the northern Pilbara samples commenced later than for other areas in the Pilbara and eastern Hamersley Basin. This may be attributed to the area, adjacent to the southern Canning Basin, having been overlain by a thicker sedimentary cover than areas more distal from the basin margin. This is supported by the 1–2.5 km-thick Ordovician-Mid Devonian sedimentary package, overlain unconformably by younger sediments adjacent to the Pilbara Craton (Figure 2).

Regionally, extensive vertical movements can be attributed to the effect of dynamic topography (Zhang et al., 2012). That is, viscous stresses created by deep mantle flow and changing mantle flow patterns that can have a profound influence on vertical motions of continental interiors, inducing surface deformation leading to dynamic topography (e.g., Braun, 2010). In our case, it is not possible to test whether the cooling episode commencing at ~420–400 Ma reported here is associated with an effect due to dynamic topography because such time-dependent models are only available from <400 Ma (Cao et al., 2019; Zhang et al., 2012). In the Paleozoic dynamic topography models of Cao et al. (2019), a vertical motion of approximately 700 m is estimated at 250 Ma for the Pilbara Craton (Figure S4). Given that heat flow in the Pilbara Craton is very low (~30–50 mW/m^2; Cull, 1982), any cooling that would accompany such a vertical change would only amount to a few degrees and would not be detected by our data. Further, surface uplift of the craton itself would have to be accompanied by some exhumation to generate a cooling signal. As such, it is difficult to assess the potential contribution of dynamic topography in early Paleozoic time.

Further, we recognize that glacially striated basement rocks and intraformational glacial striae in Permian sandstone demonstrate that glacial erosion related to the pervasive Permo-Carboniferous glaciation of Gondwana extended as far as the Pilbara Craton and the onshore Canning Basin (Gzhelian-Sakmarian ca. 305–285 Ma; Mory et al., 2008). Evidence for Permo-Carboniferous glaciation also indicates that at least in some parts of the Pilbara Craton (particularly in the northeast) and the onshore Canning Basin rocks were exposed at the surface and lacked any sedimentary cover at that time. Evidence for Permo-Carboniferous glacial features in parts of the currently exposed Pilbara Craton is in accord with our time-temperature models (Figures 8 and 9) and are essentially independent of using a time-temperature constraint. This finding supports a case that some of the rocks studied were exposed at the surface at that time. Furthermore, there is no evidence in our models for a well-defined post-Permo-Carboniferous glaciation cooling episode, having triggered a significant isostatic response over a large area of the shield, which might be related to the waxing and waning of the ice sheet.

7.2. Magnitude of Paleozoic Cooling

Results from the joint thermal history modeling based on low-temperature thermochronology data indicate a cooling episode based on expected model data of ~50–70°C, typically ranging from ~100 ± 10°C to 30 ± 10°C (Figures 8 and 9), although the addition of ZHe data in Figure 8f suggests that cooling may have proceeded from a higher temperature. Present-day heat flow data from the Western Australia shield are somewhat sparse and range from ~30–50 mW/m^2 (Cull, 1982; Morgan, 2000). This falls in the range reported from Archean terranes globally (e.g., Jaupart & Mareschal, 1999). Based on the present-day thermal regime, an estimated geothermal gradient of ~15–20°C/km would require the removal of somewhere between ~4.5–2.5 km of section to provide the interpreted Paleozoic cooling signal. More robust methods that convert thermochronometric age to erosion rate cannot be readily used in this study as such calculations can only be applied to active tectonic environments where erosion is ongoing (Willett & Brandon, 2013). However, we also recognize that estimates of the amount of the denudation would differ depending on the geothermal gradient that prevailed at the time of cooling and the thermal conductivity of any removed cover material (e.g., Braun et al., 2016; Łuszczak et al., 2017). Sedimentary rocks commonly have a range of thermal conductivities (e.g., Blackwell & Steele, 1989), which may be lower relative to basement rocks, and therefore, a relatively thick sedimentary section might display higher thermal gradients. Cull and Conley (1983) estimated that the temperature at depth may be increased by ~16–40°C/km of sedimentary rock cover. Moreover, since the evidence presented here suggests that the Paleozoic cooling event was associated with the denudation of a sedimentary cover, not the crystalline basement itself, it is important to estimate the magnitude of possible denudation under contrasting scenarios. That is, considering different basal heat flow values and the effect of a preexisting sedimentary blanket. To do so, we solved the steady-state, heat transfer equation in one dimension (vertical) within a layered crust using the Underworld Geodynamics modeling package (Beucher et al., 2019). A description of the numerical modeling can be found in the supporting

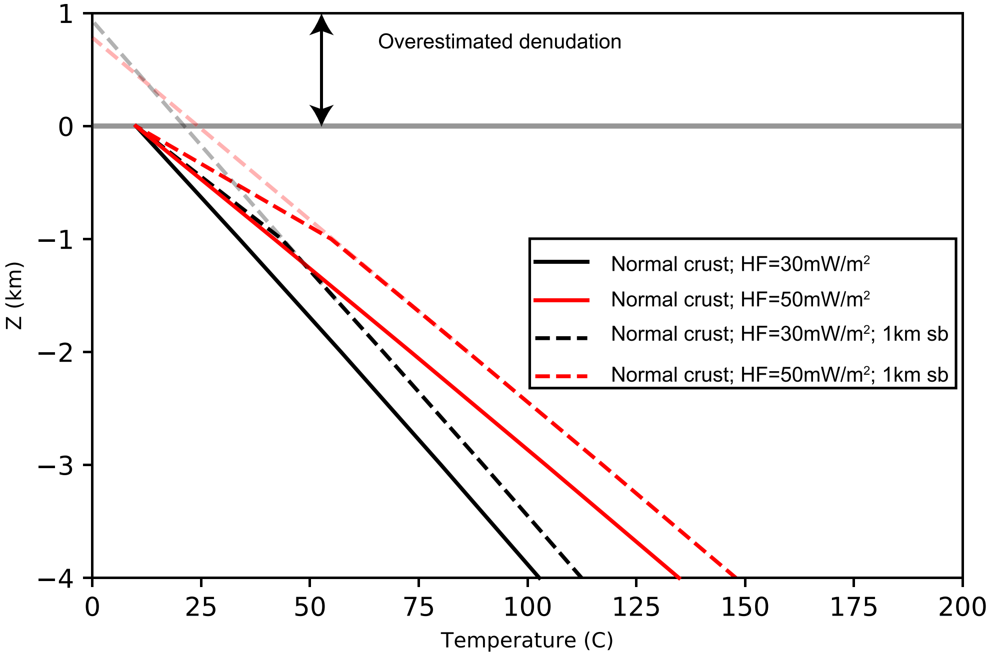

Figure 12. Change of temperature with depth for models with different crustal compositions and heat flows within the range of values measured for both global and Australian Archean cratons (Cull, 1982; Davies, 2013). Opaque dashed lines indicate predicted denudation if blanketing layer is not accounted for. HF = heat flow; sb = sediment blanket. See data repository for details of the parameters used for the 1-D heat transfer modeling.

information. Results of the 1-D model show that the approximate amount of denudation may be overestimated by >1 km if the blanketing effect is not considered (Figure 12).

8. Conclusions

Inverse thermal history modeling of low-temperature thermochronology data from a spatially extensive (~118,000 km^2) sample set across the archetypal Pilbara Craton and adjacent terranes, Australia, reveals a widespread cooling episode mostly ranging from ~420 to 300 Ma. This phase, involving at least ~50–70°C of cooling, is interpreted to be the result of unroofing of more readily erodible strata overlying the crystalline cratonic rocks. The cooling is most commonly observed over most of the Pilbara Craton and eastern Hamersley Basin, but not in the westernmost Pilbara Craton and central Hamersley Basin where cooling appears to have commenced in the late Neoproterozoic and continued at a slow rate through to the present. We attribute the areal differences in cooling history observed to variations in the thickness of sedimentary cover removed and their proximity to the adjacent rift basin. We propose that the unroofed sediments were primarily deposited in the adjacent Canning Basin. From the model-predicted cooling magnitudes, it is estimated that between ~4.5 and 2.5 km of strata may have been unroofed from this region. This range, however, depends on whether different heat flow and conductivity values are considered, with the largest difference in estimates related to the low conductivity of sediments and the thermal effect of such a sedimentary blanket on the underlying crystalline basement.

The timing of the cooling episode is coeval with the Ordovician-Carboniferous Alice Springs Orogeny, an episodic intraplate tectonic event thought to be related to a combination of far-field stresses and localization of deformation associated with thermal weakening or with regions of contrasting strengths. Previous numerical modeling provides an explanation for how a thin viscous sheet and far-field compressional forces generate compression and uplift for the orogeny as well as extension in the adjacent Canning Basin. We propose that the basin opening triggered changes in base level, which in turn resulted in denudation of the sedimentary cover in the adjoining Pilbara region leaving a record of cooling in the underlying cratonic bedrock. Our results support the view that cratons have experienced geomorphic changes during the Phanerozoic and that stresses arising from far-field deformation can be transmitted to cratons over hundreds of kilometers.

Data Availability Statement

Raw data and additional files supporting our analyses and conclusions can be found in the supporting information and a data repository (hosted at the following link https://github.com/saraemp/10.1029-2019TC005988)

Acknowledgments
This research was supported by Australian Research Council's ITRH Project IH130200012. S. M. acknowledges support from The University of Melbourne Early Career Researcher Grant Scheme. P. A. C. acknowledges support from Australian Research Council Grant FL160100168. The University of Melbourne thermochronology laboratory receives support under the AuScope program of the National Collaborative Research Infrastructure Strategy (NCRIS). Abaz Alimanović provided technical assistance with (U-Th)/He analyses. We thank Martin Danišík, an anonymous reviewer and Associate Editor Eva Enkelmann for their constructive reviews.

References

Alessio, B. L., Glorie, S., Collins, A. S., Jourdan, F., Jepson, G., Nixon, A., et al. (2019). The thermo-tectonic evolution of the southern Congo Craton margin as determined from apatite and muscovite thermochronology. *Tectonophysics*, *766*, 398–415. https://doi.org/10.1016/j.tecto.2019.06.004

Ault, A. K., & Flowers, R. M. (2012). Is apatite U-Th zonation information necessary for accurate interpretation of apatite (U-Th)/He thermochronometry data? *Geochimica et Cosmochimica Acta*, *79*, 60–78. https://doi.org/10.1016/j.gca.2011.11.037

Ault, A. K., Flowers, R. M., & Bowring, S. A. (2009). Phanerozoic burial and unroofing history of the western Slave craton and Wopmay orogen from apatite (U-Th)/He thermochronometry. *Earth and Planetary Science Letters*, *284*(1-2), 1–11. https://doi.org/10.1016/j.epsl.2009.02.035

Ault, A. K., Flowers, R. M., & Bowring, S. A. (2013). Phanerozoic surface history of the Slave craton. *Tectonics*, *32*, 1066–1083. https://doi.org/10.1002/tect.20069

Barbarand, J., Carter, A., Wood, I., & Hurford, T. (2003). Compositional and structural control of fission-track annealing in apatite. *Chemical Geology*, *198*(1-2), 107–137. https://doi.org/10.1016/S0009-2541(02)00424-2

Bargnesi, E. A., Stockli, D. F., Hourigan, J. K., & Hager, C. (2016). Improved accuracy of zircon (U-Th)/He ages by rectifying parent nuclide zonation with practical methods. *Chemical Geology*, *426*, 158–169. https://doi.org/10.1016/j.chemgeo.2016.01.017

Baughman, J. S., & Flowers, R. M. (2018). Deciphering a 2 gyr-long thermal history from a multichronometer (U-Th)/He study of the Phalaborwa Carbonatite, Kaapvaal Craton, South Africa. *Geochemistry, Geophysics, Geosystems*, *19*, 1581–1594. https://doi.org/10.1029/2017gc007198

Belton, D. X., & Raab, M. J. (2010). Cretaceous reactivation and intensified erosion in the Archean-Proterozoic Limpopo Belt, demonstrated by apatite fission track thermochronology. *Tectonophysics*, *480*(1-4), 99–108. https://doi.org/10.1016/j.tecto.2009.09.018

Beucher, R., Brown, R. W., Roper, S., Stuart, F., & Persano, C. (2013). Natural age dispersion arising from the analysis of broken crystals: Part II. Practical application to apatite (U-Th)/He thermochronometry. *Geochimica et Cosmochimica Acta*, *120*, 395–416. https://doi.org/10.1016/j.gca.2013.05.042

Beucher, R., Moresi, L., Giordani, J., Mansour, J., Sandiford, D., Farrington, R., et al. (2019). UWGeodynamics: A teaching and research tool for numerical geodynamic modelling. *Journal of Open Source Software*, *4*(36), 1136. https://doi.org/10.21105/joss.01136

Blackwell, D. D., & Steele, J. L. (1989). Thermal conductivity of sedimentary rocks: Measurement and significance. In N. D. Naeser & T. H. McCulloh (Eds.), *Thermal history of sedimentary basins*. New York, NY: Springer. https://doi.org/10.1007/978-1-4612-3492-0_2

Blum, M. D., Milliken, K., Pecha, M. A., Snedden, J. W., Frederick, B. C., & Galloway, W. E. (2017). Detrital-zircon records of Cenomanian, Paleocene, and Oligocene Gulf of Mexico drainage integration and sediment routing: Implications for scales of basin-floor fans. *Geosphere*, *13*(6), 2169–2205. https://doi.org/10.1130/GES01410.1

Boone, S. C., Seiler, C., Kohn, B. P., Gleadow, A. J. W., Foster, D. A., & Chung, L. (2018). Influence of rift superposition on lithospheric response to east African rift system extension: Lapur Range, Turkana, Kenya. *Tectonics*, *37*, 182–207. https://doi.org/10.1002/2017TC004575

Bowring, S. A., & Williams, I. S. (1999). Priscoan (4.00–4.03 Ga) orthogneisses from northwestern Canada. *Contributions to Mineralogy and Petrology*, *134*(1), 3–16. https://doi.org/10.1007/s004100050465

Braun, J. (2010). The many surface expressions of mantle dynamics. *Nature Geoscience*, *3*(12), 825–833. https://doi.org/10.1038/ngeo1020

Braun, J., Stippich, C., & Glasmacher, U. A. (2016). The effect of variability in rock thermal conductivity on exhumation rate estimates from thermochronological data. *Tectonophysics*, *690*, 288–297. https://doi.org/10.1016/j.tecto.2016.09.027

Brown, R. W., Beucher, R., Roper, S., Persano, C., Stuart, F., & Fitzgerald, P. (2013). Natural age dispersion arising from the analysis of broken crystals. Part I: Theoretical basis and implications for the apatite (U-Th)/He thermochronometer. *Geochimica et Cosmochimica Acta*, *122*, 478–497. https://doi.org/10.1016/j.gca.2013.05.041

Brown, R. W., Summerfield, M. A., & Gleadow, A. J. W. (1994). Apatite fission track analysis: Its potential for the estimation of denudation rates and implications of long-term landscape development. In M. J. Kirkby (Ed.), *Process Models and Theoretical Geomorphology* (pp. 23–53). Hoboken: Wiley.

Buick, I. S., Storkey, A., & Williams, I. S. (2008). Timing relationships between pegmatite emplacement, metamorphism and deformation during the intra-plate Alice Springs Orogeny, central Australia. *Journal of Metamorphic Geology*, *26*(9), 915–936. https://doi.org/10.1111/j.1525-1314.2008.00794.x

Burtner, R. L., Nigrini, A., & Donelick, R. A. (1994). Thermochronology of Lower Cretaceous source rocks in the Idaho-Wyoming Thrust Belt 1. *American Association of Petroleum Geologists Bulletin*, *78*(10), 1613–1636. https://doi.org/10.1306/a25ff233-171b-11d7-8645000102c1865d

Camacho, A., Hensen, B., & Armstrong, R. (2002). Isotopic test of a thermally driven intraplate orogenic model, Australia. *Geology*, *30*(10), 887–890. https://doi.org/10.1130/0091-7613(2002)030<0887:ITOATD>2.0.CO;2

Cao, W., Flament, N., Zahirovic, S., Williams, S., & Müller, R. D. (2019). The interplay of dynamic topography and eustasy on continental flooding in the late Paleozoic. *Tectonophysics*, *761*, 108–121. https://doi.org/10.1016/j.tecto.2019.04.018

Carlson, W. D., Donelick, R. A., & Ketcham, R. A. (1999). Variability of apatite fission-track annealing kinetics: I. Experimental results. *American Mineralogist*, *84*(9), 1213–1223. https://doi.org/10.2138/am-1999-0901

Cartwright, I., Buick, I. S., Foster, D. A., & Lambert, D. D. (1999). Alice Springs age shear zones from the southeastern Reynolds Range, central Australia. *Australian Journal of Earth Sciences*, *46*(3), 355–363. https://doi.org/10.1046/j.1440-0952.1999.00710.x

Cawood, P. A., Hawkesworth, C., & Dhuime, B. (2013). The continental record and the generation of continental crust. *GSA Bulletin*, *125*(1–2), 14–32. https://doi.org/10.1130/B30722.1

Cawood, P. A., & Korsch, R. J. (2008). Assembling Australia: Proterozoic building of a continent. *Precambrian Research*, *166*(1-4), 1–35. https://doi.org/10.1016/j.precamres.2008.08.006

Cawood, P. A., & Nemchin, A. A. (2000). Provenance record of a rift basin: U/Pb ages of detrital zircons from the Perth Basin, Western Australia. *Sedimentary Geology*, *134*(3-4), 209–234. https://doi.org/10.1016/S0037-0738(00)00044-0

Cawood, P. A., & Tyler, I. M. (2004). Assembling and reactivating the Proterozoic Capricorn Orogen: Lithotectonic elements, orogenies, and significance. *Precambrian Research*, *128*(3–4), 201–218. https://doi.org/10.1016/j.precamres.2003.09.001

Chaumont, J., Soulet, S., Krupa, J. C., & Carpena, J. (2002). Competition between disorder creation and annealing in fluoroapatite nuclear waste forms. *Journal of Nuclear Materials*, *301*(2-3), 122–128. https://doi.org/10.1016/S0022-3115(01)00758-9

Collins, W. J., & Shaw, R. D. (1995). Geochronological constraints on orogenic events in the Arunta Inlier: A review. *Precambrian Research*, *71*(1-4), 315–346. https://doi.org/10.1016/0301-9268(94)00067-2

Cull, J. P. (1982). *An appraisal of Australian heat-flow data* (Vol. 7, pp. 11–21). Bureau of Mineral Resources, Geology and Geophysics.

Cull, J. P., & Conley, D. (1983). Geothermal gradients and heat flow in Australian sedimentary basins. *Bureau of Mineral Resources, Geology and Geophysics*, *8*, 329–337.

Danišík, M., McInnes, B. I., Kirkland, C. L., McDonald, B. J., Evans, N. J., & Becker, T. (2017). Seeing is believing: Visualization of He distribution in zircon and implications for thermal history reconstruction on single crystals. *Science Advances*, *3*(2), e1601121. https://doi.org/10.1126/sciadv.1601121

Danišík, M., Pfaff, K., Evans, N. J., Manoloukos, C., Staude, S., McDonald, B. J., & Markl, G. (2010). Tectonothermal history of the Schwarzwald Ore District (Germany): An apatite triple dating approach. *Chemical Geology*, *278*(1–2), 58–69. https://doi.org/10.1016/j.chemgeo.2010.08.022

Danišík, M., Sachsenhofer, R. F., Privalov, V. A., Panova, E. A., Frisch, W., & Spiegel, C. (2008). Low-temperature thermal evolution of the Azov Massif (Ukrainian Shield-Ukraine)—Implications for interpreting (U-Th)/He and fission track ages from cratons. *Tectonophysics*, *456*(3-4), 171–179. https://doi.org/10.1016/j.tecto.2008.04.022

Davies, J. H. (2013). Global map of solid Earth surface heat flow. *Geochemistry, Geophysics, Geosystems*, *14*, 4608–4622. https://doi.org/10.1002/ggge.20271

de Wit, M. J., Roering, C., Hart, R. J., Armstrong, R. A., de Ronde, C. E. J., Green, R. W. E., et al. (1992). Formation of an Archaean continent. *Nature*, *357*(6379), 553–562. https://doi.org/10.1038/357553a0

Dhuime, B., Hawkesworth, C. J., Storey, C. D., & Cawood, P. A. (2011). From sediments to their source rocks: Hf and Nd isotopes in recent river sediments. *Geology*, *39*(4), 407–410. https://doi.org/10.1130/g31785.1

Djimbi, D. M., Gautheron, C., Roques, J., Tassan-Got, L., Gerin, C., & Simoni, E. (2015). Impact of apatite chemical composition on (U-Th)/He thermochronometry: An atomistic point of view. *Geochimica et Cosmochimica Acta*, *167*, 162–176. https://doi.org/10.1016/j.gca.2015.06.017

Dobson, K. J., Stuart, F. M., & Dempster, T. J. (2008). U and Th zonation in fish canyon tuff zircons: Implications for a zircon (U-Th)/He standard. *Geochimica et Cosmochimica Acta*, *72*(19), 4745–4755. https://doi.org/10.1016/j.gca.2008.07.015

Donelick, R. A., Ketcham, R. A., & Carlson, W. D. (1999). Variability of apatite fission-track annealing kinetics: II. Crystallographic orientation effects. *American Mineralogist*, *84*, 1224–1234.

Donelick, R. A., O'Sullivan, P. B., & Ketcham, R. A. (2005). Apatite fission-track analysis. *Reviews in Mineralogy and Geochemistry*, *58*(1), 49–94. https://doi.org/10.2138/rmg.2005.58.3

Donelick, R. A., O'Sullivan, P. B., Ketcham, R. A., Hendriks, B. W. H., & Redfield, T. F. (2006). Relative U and Th concentrations from LA-ICP-MS for apatite fission-track grain-age dating. *Geochimica et Cosmochimica Acta*, *70*(18, Supplement), A143. https://doi.org/10.1016/j.gca.2006.06.1595

Driscoll, N. W., & Karner, G. D. (1998). Lower crustal extension across the Northern Carnarvon basin, Australia: Evidence for an eastward dipping detachment. *Journal of Geophysical Research*, *103*(B3), 4975–4991. https://doi.org/10.1029/97JB03295

Enkelmann, E., & Garver, J. I. (2016). Low-temperature thermochronology applied to ancient settings. *Journal of Geodynamics*, *93*, 17–30. https://doi.org/10.1016/j.jog.2015.11.001

Farley, K., Wolf, R., & Silver, L. (1996). The effects of long alpha-stopping distances on (U-Th)/He ages. *Geochimica et Cosmochimica Acta*, *60*(21), 4223–4229. https://doi.org/10.1016/S0016-7037(96)00193-7

Farley, K. A. (2002). (U-Th)/He dating: Techniques, calibrations, and applications. *Reviews in Mineralogy and Geochemistry*, *47*(1), 819–844.

Feinstein, S., Kohn, B., Osadetz, K., Everitt, R., & O'Sullivan, P. (2009). Variable Phanerozoic thermal history in the Southern Canadian Shield: Evidence from an apatite fission track profile at the Underground Research Laboratory (URL), Manitoba. *Tectonophysics*, *475*(1), 190–199. https://doi.org/10.1016/j.tecto.2009.01.016

Ferguson, K. U. (1981). Fission track dating of shield areas. In *Relationships between tectonic and thermal histories and fission track age distributions*. Australia: University of Melbourne, unpublished MSc thesis.

Fitzgerald, P. G., Baldwin, S. L., Webb, L. E., & O'Sullivan, P. B. (2006). Interpretation of (U–Th)/He single grain ages from slowly cooled crustal terranes: A case study from the Transantarctic Mountains of southern Victoria Land. *Chemical Geology*, *225*(1-2), 91–120. https://doi.org/10.1016/j.chemgeo.2005.09.001

Flament, N., Rey, P. F., Coltice, N., Dromart, G., & Olivier, N. (2011). Lower crustal flow kept Archean continental flood basalts at sea level. *Geology*, *39*(12), 1159–1162. https://doi.org/10.1130/G32231.1

Flowers, R. M. (2009). Exploiting radiation damage control on apatite (U–Th)/He dates in cratonic regions. *Earth and Planetary Science Letters*, *277*(1–2), 148–155. https://doi.org/10.1016/j.epsl.2008.10.005

Flowers, R. M., Bowring, S. A., & Reiners, P. W. (2006). Low long-term erosion rates and extreme continental stability documented by ancient (U-Th)/He dates. *Geology*, *34*(11), 925–928. https://doi.org/10.1130/g22670a.1

Flowers, R. M., & Ehlers, T. A. (2018). Rock erodibility and the interpretation of low-temperature thermochronologic data. *Earth and Planetary Science Letters*, *482*, 312–323. https://doi.org/10.1016/j.epsl.2017.11.018

Flowers, R. M., & Kelley, S. A. (2011). Interpreting data dispersion and "inverted" dates in apatite (U–Th)/He and fission-track datasets: An example from the US midcontinent. *Geochimica et Cosmochimica Acta*, *75*(18), 5169–5186. https://doi.org/10.1016/j.gca.2011.06.016

Flowers, R. M., Ketcham, R. A., Shuster, D. L., & Farley, K. A. (2009). Apatite (U–Th)/He thermochronometry using a radiation damage accumulation and annealing model. *Geochimica et Cosmochimica Acta*, *73*(8), 2347–2365. https://doi.org/10.1016/j.gca.2009.01.015

Flowers, R. M., & Schoene, B. (2010). (U-Th)/He thermochronometry constraints on unroofing of the eastern Kaapvaal craton and significance for uplift of the southern African Plateau. *Geology*, *38*(9), 827–830. https://doi.org/10.1130/g30980.1

Flowers, R. M., Shuster, D. L., Wernicke, B. P., & Farley, K. A. (2007). Radiation damage control on apatite (U-Th)/He dates from the Grand Canyon region, Colorado Plateau. *Geology*, *35*(5), 447–450. https://doi.org/10.1130/g23471a.1

Galbraith, R. F., & Laslett, G. M. (1993). Statistical models for mixed fission track ages. *Nuclear Tracks and Radiation Measurements*, *21*(4), 459–470. https://doi.org/10.1016/1359-0189(93)90185-C

Gallagher, K. (2012). Transdimensional inverse thermal history modeling for quantitative thermochronology. *Journal of Geophysical Research*, *117*, B02408. https://doi.org/10.1029/2011JB008825

Gallagher, K., & Brown, R. (1997). The onshore record of passive margin evolution. *Journal of the Geological Society*, *154*(3), 451. https://doi.org/10.1144/gsjgs.154.3.0451

Gallagher, K., Charvin, K., Nielsen, S., Sambridge, M., & Stephenson, J. (2009). Markov chain Monte Carlo (MCMC) sampling methods to determine optimal models, model resolution and model choice for Earth Science problems. *Marine and Petroleum Geology*, *26*(4), 525–535. https://doi.org/10.1016/j.marpetgeo.2009.01.003

Gartrell, A. (2000). Rheological controls on extensional styles and the structural evolution of the northern Carnarvon Basin, North West Shelf, Australia. *Australian Journal of Earth Sciences*, *47*(2), 231–244. https://doi.org/10.1046/j.1440-0952.2000.00776.x

Gautheron, C., Barbarand, J., Ketcham, R. A., Tassan-Got, L., van der Beek, P., Pagel, M., et al. (2013). Chemical influence on α-recoil damage annealing in apatite: Implications for (U-Th)/He dating. *Chemical Geology*, *351*, 257–267. https://doi.org/10.1016/j.chemgeo.2013.05.027

Gautheron, C., Tassan-Got, L., Barbarand, J., & Pagel, M. (2009). Effect of alpha-damage annealing on apatite (U–Th)/He thermochronology. *Chemical Geology*, *266*(3–4), 157–170. https://doi.org/10.1016/j.chemgeo.2009.06.001

Gautheron, C., Tassan-Got, L., Ketcham, R. A., & Dobson, K. J. (2012). Accounting for long alpha-particle stopping distances in (U-Th-Sm)/He geochronology: 3-D modeling of diffusion, zoning, implantation, and abrasion. *Geochimica et Cosmochimica Acta*, *96*, 44–56. https://doi.org/10.1016/j.gca.2012.08.016

Gerin, C., Gautheron, C., Oliviero, E., Bachelet, C., Mbongo Djimbi, D., Seydoux-Guillaume, A.-M., et al. (2017). Influence of vacancy damage on He diffusion in apatite, investigated at atomic to mineralogical scales. *Geochimica et Cosmochimica Acta*, *197*, 87–103. https://doi.org/10.1016/j.gca.2016.10.018

Ginster, U., Reiners, P. W., & Nasdala, L. (2019). Annealing kinetics of radiation damage in zircon. *Geochimica et Cosmochimica Acta*, *249*, 225–246. https://doi.org/10.1016/j.gca.2019.01.033

Gleadow, A., Harrison, M., Kohn, B., Lugo-Zazueta, R., & Phillips, D. (2015). The Fish Canyon Tuff: A new look at an old low-temperature thermochronology standard. *Earth and Planetary Science Letters*, *424*, 95–108. https://doi.org/10.1016/j.epsl.2015.05.003

Gleadow, A. J., Belton, D. X., Kohn, B. P., & Brown, R. W. (2002). Fission track dating of phosphate minerals and the thermochronology of apatite. *Reviews in Mineralogy and Geochemistry*, *48*(1), 579–630. https://doi.org/10.2138/rmg.2002.48.16

Gleadow, A. J. W., Gleadow, S. J., Belton, D. X., Kohn, B. P., Krochmal, M. S., & Brown, R. W. (2009). Coincidence mapping—A key strategy for the automatic counting of fission tracks in natural minerals. *Geological Society, London, Special Publications*, *324*(1), 25. https://doi.org/10.1144/SP324.2

Gleadow, A. J. W., & Lovering, J. F. (1978). Thermal history of granitic rocks from western Victoria: A fission-track dating study. *Journal of the Geological Society of Australia*, *25*(5–6), 323–340. https://doi.org/10.1080/00167617808729039

Glorie, S., Agostino, K., Dutch, R., Pawley, M., Hall, J., Danišík, M., et al. (2017). Thermal history and differential exhumation across the Eastern Musgrave Province, South Australia: Insights from low-temperature thermochronology. *Tectonophysics*, *703*, 23–41.

Goodwin, A. M. (1996). *Principles of Precambrian geology* (p. 327). London: Academic Press. Retrieved from https://www.sciencedirect.com/book/9780122897702/principles-of-precambrian-geology#book-info

Green, P., & Duddy, I. (2018). Apatite (U-Th-Sm)/He thermochronology on the wrong side of the tracks. *Chemical Geology*, *488*, 21–33. https://doi.org/10.1016/j.chemgeo.2018.04.028

Green, P. F. (1986). On the thermo-tectonic evolution of Northern England: Evidence from fission track analysis. *Geological Magazine*, *123*(5), 493–506. https://doi.org/10.1017/S0016756800035081

Green, P. F., Crowhurst, P. V., Duddy, I. R., Japsen, P., & Holford, S. P. (2006). Conflicting (U-Th)/He and fission track ages in apatite: Enhanced He retention, not anomalous annealing behaviour. *Earth and Planetary Science Letters*, *250*(3-4), 407–427. https://doi.org/10.1016/j.epsl.2006.08.022

Green, P. F., & Duddy, I. R. (2006). Interpretation of apatite (U-Th)/He ages and fission track ages from cratons. *Earth and Planetary Science Letters*, *244*(3-4), 541–547. https://doi.org/10.1016/j.epsl.2006.02.024

Green, P. F., Duddy, I. R., Gleadow, A. J. W., & Lovering, J. F. (1989). Apatite fission-track analysis as a paleotemperature indicator for hydrocarbon exploration. In N. D. Naeser, & T. H. McCulloh (Eds.), *Thermal history of sedimentary basins—Methods and case histories* (pp. 181–195). New York, New York: Springer. https://doi.org/10.1007/978-1-4612-3492-0_11

Guenthner, W. R., Reiners, P. W., Drake, H., & Tillberg, M. (2017). Zircon, titanite, and apatite (U-Th)/He ages and age-eU correlations from the Fennoscandian Shield, southern Sweden. *Tectonics*, *36*, 1254–1274. https://doi.org/10.1002/2017tc004525

Guenthner, W. R., Reiners, P. W., Ketcham, R. A., Nasdala, L., & Giester, G. (2013). Helium diffusion in natural zircon: Radiation damage, anisotropy, and the interpretation of zircon (U-Th)/He thermochronology. *American Journal of Science*, *313*(3), 145–198. https://doi.org/10.2475/03.2013.01

Guenthner, W. R., Reiners, P. W., & Tian, Y. (2014). Interpreting date-eU correlations in zircon (U-Th)/He datasets: A case study from the Longmen Shan, China. *Earth and Planetary Science Letters*, *403*, 328–339. https://doi.org/10.1016/j.epsl.2014.06.050

Haines, P., Wingate, M., & Kirkland, C. (2013). Detrital zircon U-Pb ages from the Paleozoic of the Canning and Officer Basins, Western Australia: Implications for provenance and interbasin connections. Paper Presented at the Sedimentary Basins of Western Aus Tralia IV: Proceedings of the Petroleum Exploration Society of Australia Symposium, Perth, Western Australia.

Harman, R., Gallagher, K., Brown, R., Raza, A., & Bizzi, L. (1998). Accelerated denudation and tectonic/geomorphic reactivation of the cratons of northeastern Brazil during the Late Cretaceous. *Journal of Geophysical Research*, *103*(B11), 27,091–27,105. https://doi.org/10.1029/98JB02524

Hasebe, N., Barbarand, J., Jarvis, K., Carter, A., & Hurford, A. J. (2004). Apatite fission-track chronometry using laser ablation ICP-MS. *Chemical Geology*, *207*(3-4), 135–145. https://doi.org/10.1016/j.chemgeo.2004.01.007

Hashimoto, T., Bailey, A., & Chirinos, A. (2018). Onshore basin inventory volume 2: The Canning, Perth and Officer basins. Geoscience Australia.

Hendriks, B. W. H., & Redfield, T. F. (2005). Apatite fission track and (U-Th)/He data from Fennoscandia: An example of underestimation of fission track annealing in apatite. *Earth and Planetary Science Letters*, *236*(1-2), 443–458. https://doi.org/10.1016/j.epsl.2005.05.027

Hendriks, B. W. H., & Redfield, T. F. (2006). Reply to: Comment on "apatite fission track and (U-Th)/He data from Fennoscandia: An example of underestimation of fission track annealing in apatite" by B. W. H. Hendriks and T. F. Redfield. *Earth and Planetary Science Letters*, *248*(1-2), 569–577. https://doi.org/10.1016/j.epsl.2006.06.022

Hickman, A. H., & Van Kranendonk, M. J. (2012). Early Earth evolution: Evidence from the 3.5–1.8 Ga geological history of the Pilbara region of Western Australia. *Episodes*, *35*(1), 283–297.

Holbrook, J., Scott, R. W., & Oboh-Ikuenobe, F. E. (2006). Base-level buffers and buttresses: A model for upstream versus downstream control on fluvial geometry and architecture within sequences. *Journal of Sedimentary Research*, *76*(1), 162–174. https://doi.org/10.2110/jsr.2005.10

Hourigan, J. K., Reiners, P. W., & Brandon, M. T. (2005). U-Th zonation-dependent alpha-ejection in (U-Th)/He chronometry. *Geochimica et Cosmochimica Acta*, *69*(13), 3349–3365. https://doi.org/10.1016/j.gca.2005.01.024

House, M. A., Farley, K. A., & Stockli, D. (2000). Helium chronometry of apatite and titanite using Nd-YAG laser heating. *Earth and Planetary Science Letters*, *183*(3-4), 365–368. https://doi.org/10.1016/S0012-821X(00)00286-7

I'Anson, A., Elders, C., & McHarg, S. (2019). Marginal fault systems of the Northern Carnarvon Basin: Evidence for multiple Palaeozoic extension events, North-West Shelf, Australia. *Marine and Petroleum Geology*, *101*, 211–229. https://doi.org/10.1016/j.marpetgeo.2018.11.040

Jaupart, C., & Mareschal, J. C. (1999). The thermal structure and thickness of continental roots. *Lithos*, *48*(1-4), 93–114. https://doi.org/10.1016/S0024-4937(99)00023-7

Johnson, J. E., Flowers, R. M., Baird, G. B., & Mahan, K. H. (2017). "Inverted" zircon and apatite (U-Th)/He dates from the Front Range, Colorado: High-damage zircon as a low-temperature (<50 °C) thermochronometer. *Earth and Planetary Science Letters*, *466*, 80–90. https://doi.org/10.1016/j.epsl.2017.03.002

Jordan, T. H. (1978). Composition and development of the continental tectosphere. *Nature*, *274*(5671), 544–548. https://doi.org/10.1038/274544a0

Kasanzu, C. H. (2017). Apatite fission track and (U-Th)/He thermochronology from the Archean Tanzania Craton: Contributions to cooling histories of Tanzanian basement rocks. *Geoscience Frontiers*, *8*(5), 999–1007. https://doi.org/10.1016/j.gsf.2016.09.007

Kennard, J., Jackson, M., Romine, K., Shaw, R., Southgate, P., Purcell, P., & Purcell, R. (1994). Depositional sequences and associated petroleum systems of the Canning Basin, WA.

Ketcham, R. A. (2019). Fission-track annealing: From geologic observations to thermal history modeling. In M. G. Malusà, & P. G. Fitzgerald (Eds.), *Fission-track thermochronology and its application to geology* (pp. 49–75). Cham: Springer International Publishing. https://doi.org/10.1007/978-3-319-89421-8_3

Ketcham, R. A., Carter, A., Donelick, R. A., Barbarand, J., & Hurford, A. J. (2007). Improved modeling of fission-track annealing in apatite. *American Mineralogist*, *92*(5-6), 799–810. https://doi.org/10.2138/am.2007.2281

Ketcham, R. A., Gautheron, C., & Tassan-Got, L. (2011). Accounting for long alpha-particle stopping distances in (U-Th-Sm)/He geochronology: Refinement of the baseline case. *Geochimica et Cosmochimica Acta*, *75*(24), 7779–7791. https://doi.org/10.1016/j.gca.2011.10.011

Ketcham, R. A., Guenthner, W. R., & Reiners, P. W. (2013). Geometric analysis of radiation damage connectivity in zircon, and its implications for helium diffusion. *American Mineralogist*, *98*(2–3), 350–360. https://doi.org/10.2138/am.2013.4249

Kohn, B., & Gleadow, A. (2019). Application of low-temperature thermochronology to craton evolution. In M. Malusà & P. Fitzgerald (Eds.), *Fission-track thermochronology and its application to geology*, *Springer Textbooks in Earth Sciences, Geography and Environment*. Cham: Springer. https://doi.org/10.1007/978-3-319-89421-8_21

Kohn, B. P., Foster, D. A., & Farley, K. A. (2002). Low temperature thermochronology of apatite with exceptional compositional variations: The Stillwater Complex, Montana revisited. *Geotemas*, *4*, 103–105.

Kohn, B. P., Gleadow, A. J. W., Brown, R. W., Gallagher, K., Lorencak, M., & Noble, W. P. (2005). Visualizing thermotectonic and denudation histories using apatite fission track thermochronology. *Reviews in Mineralogy and Geochemistry*, *58*(1), 527–565. https://doi.org/10.2138/rmg.2005.58.20

Kohn, B. P., Gleadow, A. J. W., Brown, R. W., Gallagher, K., O'Sullivan, P. B., & Foster, D. A. (2002). Shaping the Australian crust over the last 300 million years: Insights from fission track thermotectonic imaging and denudation studies of key terranes. *Australian Journal of Earth Sciences*, *49*(4), 697–717. https://doi.org/10.1046/j.1440-0952.2002.00942.x

Kohn, B. P., Lorencak, M., Gleadow, A. J. W., Kohlmann, F., Raza, A., Osadetz, K. G., & Sorjonen-Ward, P. (2009). A reappraisal of low-temperature thermochronology of the eastern Fennoscandia Shield and radiation-enhanced apatite fission-track annealing. *Geological Society, London, Special Publications*, *324*(1), 193–216. https://doi.org/10.1144/sp324.15

Larson, S. Å., Cederbom, C. E., Tullborg, E.-L., & Stiberg, J.-P. (2006). Comment on "apatite fission track and (U-Th)/He data from Fennoscandia: An example of underestimation of fission track annealing in apatite" by Hendriks and Redfield [earth planet. Sci. Lett. 236 (443–458)]. *Earth and Planetary Science Letters*, *248*(1-2), 561–568. https://doi.org/10.1016/j.epsl.2006.06.018

Larson, S. Å., Tullborg, E.-L., Cederbom, C., & Stiberg, J.-P. (1999). Sveconorwegian and Caledonian foreland basins in the Baltic Shield revealed by fission-track thermochronology. *Terra Nova*, *11*, 210–215. https://doi.org/10.1046/j.1365-3121.1999.00249.x

Lee, C.-T. A., Caves, J., Jiang, H., Cao, W., Lenardic, A., McKenzie, N. R., et al. (2018). Deep mantle roots and continental emergence: Implications for whole-Earth elemental cycling, long-term climate, and the Cambrian explosion. *International Geology Review*, *60*(4), 431–448.2017.1340853. https://doi.org/10.1080/00206814.2017.1340853

Lenardic, A., Moresi, L., & Mühlhaus, H. (2000). The role of mobile belts for the longevity of deep cratonic lithosphere: The crumple zone model. *Geophysical Research Letters*, *27*(8), 1235–1238. https://doi.org/10.1029/1999GL008410

Lewis, C., Sircombe, K., Keep, M., & Moss, S. (2013). *Use of U-Pb geochronology to delineate provenance of North West Shelf sediments, Australia* (pp. 1–27). Paper presented at the Sedimentary Basins of Western Australia IV: Proceedings of the Petroleum Exploration Society of Australia Symposium, Perth, Western Australia.

Łuszczak, K., Persano, C., Braun, J., & Stuart, F. M. (2017). How local crustal thermal properties influence the amount of denudation derived from low-temperature thermochronometry. *Geology*, *45*(9), 779–782. https://doi.org/10.1130/G39036.1

Mackintosh, V., Kohn, B., Gleadow, A., & Belton, D. X. (2019). Thermochronological insights into the morphotectonic evolution of the Eastern Highlands, Zimbabwe: Implications for thermal history modelling of multi-thermochronometer data. *Journal of African Earth Sciences*, *158*, 103542. https://doi.org/10.1016/j.jafrearsci.2019.103542

Mackintosh, V., Kohn, B., Gleadow, A., & Tian, Y. (2017). Phanerozoic morphotectonic evolution of the Zimbabwe Craton: Unexpected outcomes from a multiple low-temperature thermochronology study. *Tectonics*, *36*, 2044–2067. https://doi.org/10.1002/2017TC004703

Martin, J., Fernandes, A. M., Pickering, J., Howes, N., Mann, S., & McNeil, K. (2018). The stratigraphically preserved signature of persistent backwater dynamics in a large paleodelta system: The Mungaroo Formation, North West Shelf, Australia. *Journal of Sedimentary Research*, *88*(7), 850–872. https://doi.org/10.2110/jsr.2018.38

Mason, C. C., Romans, B. W., Stockli, D. F., Mapes, R. W., & Fildani, A. (2019). Detrital zircons reveal sea-level and hydroclimate controls on Amazon River to deep-sea fan sediment transfer. *Geology*, *47*(6), 563–567. https://doi.org/10.1130/g45852.1

McDannell, K. T., Issler, D. R., & O'Sullivan, P. B. (2019). Radiation-enhanced fission track annealing revisited and consequences for apatite thermochronometry. *Geochimica et Cosmochimica Acta*, *252*, 213–239. https://doi.org/10.1016/j.gca.2019.03.006

McDannell, K. T., Zeitler, P. K., Janes, D. G., Idleman, B. D., & Fayon, A. K. (2018). Screening apatites for (U-Th)/He thermochronometry via continuous ramped heating: He age components and implications for age dispersion. *Geochimica et Cosmochimica Acta*, *223*, 90–106. https://doi.org/10.1016/j.gca.2017.11.031

McDowell, F. W., McIntosh, W. C., & Farley, K. A. (2005). A precise 40Ar–39Ar reference age for the Durango apatite (U-Th)/He and fission-track dating standard. *Chemical Geology*, *214*(3-4), 249–263. https://doi.org/10.1016/j.chemgeo.2004.10.002

Meesters, A. G. C. A., & Dunai, T. J. (2002). Solving the production-diffusion equation for finite diffusion domains of various shapes: Part I. implications for low-temperature (U-Th)/He thermochronology. *Chemical Geology*, *186*(3-4), 333–344. https://doi.org/10.1016/S0009-2541(01)00422-3

Morgan, P. (2000). Heat flow. In J. J. Veevers (Ed.), *Billion-year earth history of Australia and neighbours in Gondwanaland* (pp. 82–90). Sydney: GEMOC Press.

Morón, S., Cawood, P. A., Haines, P. W., Gallagher, S. J., Zahirovic, S., Lewis, C. J., & Moresi, L. (2019). Long-lived transcontinental sediment transport pathways of East Gondwana. *Geology*, *47*(6), 513–516. https://doi.org/10.1130/g45915.1

Mory, A., Redfern, J., & Martin, J. (2008). A review of Permian-Carboniferous glacial deposits in Western Australia. *Geological Society of America Special Papers*, *441*, 29–40.

Mory, A. J., & Haines, P. W. (2013). A Paleozoic perspective of Western Australia. In M. Keep, & S. J. Moss (Eds.), *The Sedimentary Basins of Western Australia IV* (pp. 1–25). Perth, WA: Petroleum Exploration Society of Australia.

Murray, K. E., Orme, D. A., & Reiners, P. W. (2014). Effects of U-Th-rich grain boundary phases on apatite helium ages. *Chemical Geology*, *390*, 135–151. https://doi.org/10.1016/j.chemgeo.2014.09.023

Myers, J. S., Shaw, R. D., & Tyler, I. M. (1996). Tectonic evolution of proterozoic Australia. *Tectonics*, *15*(6), 1431–1446. https://doi.org/10.1029/96TC02356

Orme, D. A., Guenthner, W. R., Laskowski, A. K., & Reiners, P. W. (2016). Long-term tectonothermal history of Laramide basement from zircon-He age-eU correlations. *Earth and Planetary Science Letters*, *453*, 119–130. https://doi.org/10.1016/j.epsl.2016.07.046

Oversby, V. (1976). Isotopic ages and geochemistry of Archaean acid igneous rocks from the Pilbara, Western Australia. *Geochimica et Cosmochimica Acta*, *40*(7), 817–829. https://doi.org/10.1016/0016-7037(76)90034-X

Paton, C., Hellstrom, J., Paul, B., Woodhead, J., & Hergt, J. (2011). Iolite: Freeware for the visualisation and processing of mass spectrometric data. *Journal of Analytical Atomic Spectrometry*, *26*(12), 2508–2518. https://doi.org/10.1039/C1JA10172B

Pinet, N. (2016). Far-field effects of Appalachian orogenesis: A view from the craton. *Geology*, *44*(2), 83–86. https://doi.org/10.1130/g37356.1

Pollack, H. N. (1986). Cratonization and thermal evolution of the mantle. *Earth and Planetary Science Letters*, *80*(1–2), 175–182. https://doi.org/10.1016/0012-821X(86)90031-2

Quidelleur, X., Grove, M., Lovera, O. M., Harrison, T. M., Yin, A., & Ryerson, F. (1997). Thermal evolution and slip history of the Renbu Zedong Thrust, southeastern Tibet. *Journal of Geophysical Research*, *102*(B2), 2659–2679. https://doi.org/10.1029/96JB02483

Recanati, A., Gautheron, C., Barbarand, J., Missenard, Y., Pinna-Jamme, R., Tassan-Got, L., et al. (2017). Helium trapping in apatite damage: Insights from (U-Th-Sm)/He dating of different granitoid lithologies. *Chemical Geology*, *470*, 116–131. https://doi.org/10.1016/j.chemgeo.2017.09.002

Reiners, P. W. (2005). Zircon (U-Th)/He thermochronometry. *Reviews in Mineralogy and Geochemistry*, *58*(1), 151–179. https://doi.org/10.2138/rmg.2005.58.6

Reiners, P. W., Carlson, R. W., Renne, P. R., Cooper, K. M., Granger, D. E., McLean, N. M., & Schoene, B. (2018). *Geochronology and thermochronology*, Hoboken, NJ: John Wiley and Sons Ltd.

Reiners, P. W., & Farley, K. A. (2001). Influence of crystal size on apatite (U-Th)/He thermochronology: An example from the Bighorn Mountains, Wyoming. *Earth and Planetary Science Letters*, *188*(3-4), 413–420. https://doi.org/10.1016/S0012-821X(01)00341-7

Roberts, E. A., & Houseman, G. A. (2001). Geodynamics of central Australia during the intraplate Alice Springs Orogeny: Thin viscous sheet models. *Geological Society, London, Special Publications*, *184*(1), 139–164. https://doi.org/10.1144/GSL.SP.2001.184.01.08

Romine, K. K., Southgate, P. N., Kennard, J. M., & Jackson, M. J. (1994). The Ordovician to Silurian phase of the Canning Basin, WA: Structure and sequence evolution. In P. G. Purcell, & R. R. Purcell (Eds.), *The sedimentary basins of Western Australia* (pp. 677–696). Western Australia: petroleum exploration Society of Australia.

Schneider, D. A., & Issler, D. R. (2019). Application of low-temperature thermochronology to hydrocarbon exploration. In M. G. Malusà, & P. G. Fitzgerald (Eds.), *Fission-Track Thermochronology and its Application to Geology* (pp. 315–333). New York: Springer International Publishing. https://doi.org/10.1007/978-3-319-89421-8_18

Seiler, C., Kohn, B. P., & Gleadow, A. (2014). Apatite fission track analysis by LA-ICP-MS: An evaluation of the absolute dating approach. Paper presented at 14th International Conference on Thermochronology, Chamonix.

Shaw, R. D., Sexton, M. J., & Zeilinger, I. (1995). *The tectonic framework of the Canning Basin, W.A., including 1: 2 million structural elements map of the Canning Basin*. Canberra: Australian Geological Survey Organisation.

Shaw, R. D., Etheridge, M. A., & Lambeck, K. (1991). Development of the late Proterozoic to mid-Paleozoic, intracratonic Amadeus Basin in Central Australia: A key to understanding tectonic forces in plate interiors. *Tectonics*, *10*(4), 688–721. https://doi.org/10.1029/90tc02417

Shuster, D. L., Flowers, R. M., & Farley, K. A. (2006). The influence of natural radiation damage on helium diffusion kinetics in apatite. *Earth and Planetary Science Letters*, *249*(3–4), 148–161. https://doi.org/10.1016/j.epsl.2006.07.028

Sircombe, K., & Freeman, M. (1999). Provenance of detrital zircons on the Western Australia coastline—Implications for the geologic history of the Perth basin and denudation of the Yilgarn craton. *Geology*, *27*(10), 879–882. https://doi.org/10.1130/0091-7613(1999)027<0879:PODZOT>2.3.CO;2

Spiegel, C., Kohn, B., Belton, D., Berner, Z., & Gleadow, A. (2009). Apatite (U-Th-Sm)/He thermochronology of rapidly cooled samples: The effect of He implantation. *Earth and Planetary Science Letters*, *285*(1-2), 105–114. https://doi.org/10.1016/j.epsl.2009.05.045

Stokes, M., & Mather, A. E. (2000). Response of Plio-Pleistocene alluvial systems to tectonically induced base-level changes, Vera Basin, SE Spain. *Journal of the Geological Society*, *157*(2), 303–316. https://doi.org/10.1144/jgs.157.2.303

Veevers, J. J., Saeed, A., Belousova, E. A., & Griffin, W. L. (2005). U-Pb ages and source composition by Hf-isotope and trace-element analysis of detrital zircons in Permian sandstone and modern sand from southwestern Australia and a review of the paleogeographical and denudational history of the Yilgarn Craton. *Earth-Science Reviews*, *68*(3-4), 245–279. https://doi.org/10.1016/j.earscirev.2004.05.005

Vermeesch, P. (2009). RadialPlotter: A Java application for fission track, luminescence and other radial plots. *Radiation Measurements*, *44*(4), 409–410. https://doi.org/10.1016/j.radmeas.2009.05.003

Vermeesch, P., Seward, D., Latkoczy, C., Wipf, M., Günther, D., & Baur, H. (2007). α-Emitting mineral inclusions in apatite, their effect on (U-Th)/He ages, and how to reduce it. *Geochimica et Cosmochimica Acta*, *71*(7), 1737–1746. https://doi.org/10.1016/j.gca.2006.09.020

Weber, U., Kohn, B., Gleadow, A., & Nelson, D. (2005). Low temperature Phanerozoic history of the Northern Yilgarn Craton, Western Australia. *Tectonophysics*, *400*(1–4), 127–151. https://doi.org/10.1016/j.tecto.2005.03.008

Weber, U. D. (2002). The thermotectonic evolution of the northern Precambrian Shield, Western Australia. PhD thesis, University of Melbourne, Australia.

Wildman, M., Brown, R., Beucher, R., Persano, C., Stuart, F., Gallagher, K., et al. (2016). The chronology and tectonic style of landscape evolution along the elevated Atlantic continental margin of South Africa resolved by joint apatite fission track and (U-Th-Sm)/He thermochronology. *Tectonics*, *35*, 511–545. https://doi.org/10.1002/2015TC004042

Wildman, M., Brown, R., Persano, C., Beucher, R., Stuart, F. M., Mackintosh, V., et al. (2017). Contrasting Mesozoic evolution across the boundary between on and off craton regions of the South African plateau inferred from apatite fission track and (U-Th-Sm)/He thermochronology. *Journal of Geophysical Research: Solid Earth*, *122*, 1517–1547. https://doi.org/10.1002/2016JB013478

Wildman, M., Cogné, N., & Beucher, R. (2019). Fission-track thermochronology applied to the evolution of passive continental margins. In M. G. Malusà, & P. G. Fitzgerald (Eds.), *Fission-track thermochronology and its application to geology* (pp. 351–371). Cham: Springer International Publishing. https://doi.org/10.1007/978-3-319-89421-8_20

Willett, S. D., & Brandon, M. T. (2013). Some analytical methods for converting thermochronometric age to erosion rate. *Geochemistry, Geophysics, Geosystems*, *14*, 209–222. https://doi.org/10.1029/2012GC004279

Wolfe, M. R., & Stockli, D. F. (2010). Zircon (U-Th)/He thermochronometry in the KTB drill hole, Germany, and its implications for bulk He diffusion kinetics in zircon. *Earth and Planetary Science Letters*, *295*(1–2), 69–82. https://doi.org/10.1016/j.epsl.2010.03.025

Yeh, M.-W., & Shellnutt, J. G. (2016). The initial break-up of Pangæa elicited by Late Palaeozoic deglaciation. *Scientific Reports*, *6*(1), 31,442. https://doi.org/10.1038/srep31442

Zeitler, P. K., Enkelmann, E., Thomas, J. B., Watson, E. B., Ancuta, L. D., & Idleman, B. D. (2017). Solubility and trapping of helium in apatite. *Geochimica et Cosmochimica Acta*, *209*, 1–8. https://doi.org/10.1016/j.gca.2017.03.041

Zhang, N., Zhong, S., & Flowers, R. M. (2012). Predicting and testing continental vertical motion histories since the Paleozoic. *Earth and Planetary Science Letters*, *317-318*, 426–435. https://doi.org/10.1016/j.epsl.2011.10.041